International Journal of Thermal Sciences 220 (2026) 110275



Contents lists available at ScienceDirect

International Journal of Thermal Sciences

journal homepage: www.elsevier.com/locate/ijts



Thermodynamic and magneto-convective performance of Fe_3O_4-Al_2O_3–MWCNT ternary nanofluids in transitional flow regimes

Victor O. Adogbeji [a,b,*], Tartibu Lagouge [a], Mohsen Sharifpur [b,c,d,**], Josua P. Meyer [b,e]

[a] Department of Mechanical and Industrial Engineering Technology, University of Johannesburg, Private Bag, Johannesburg, 2092, South Africa
[b] Department of Mechanical and Aeronautical Engineering, University of Pretoria, Pretoria, Private Bag X20, Hatfield, 0028, South Africa
[c] School of Mechanical, Industrial and Aeronautical Engineering, University of the Witwatersrand, Private Bag 3, Wits, 2050, South Africa
[d] Department of Medical Research, China Medical University, China Medical University Hospital Taichung, Taiwan
[e] Department of Mechanical and Mechatronic Engineering, Stellenbosch University, Stellenbosch, South Africa

ARTICLE INFO

Keywords:
Entropy generation
Magnetohydrodynamic effect
Ternary hybrid nanofluids
Thermal efficiency index
Transition flow regime
Waveform optimization

ABSTRACT

The design of advanced heat transfer fluids plays a vital role in improving the thermal efficiency of next-generation cooling systems. This study presents an experimental investigation into the magneto-thermal behavior of a ternary hybrid nanofluid (THNF) formulated from Fe_3O_4, Al_2O_3, and multi-walled carbon nanotubes (MWCNTs) dispersed in deionized water (DIW). The study spans transitional and turbulent flow regimes (Re 2300–7000) with nanoparticle volume fractions ranging from 0.025 % to 0.4 %. In the transitional regime, the ternary nanofluid achieved a peak Nusselt number enhancement of 29.49 % at 0.05 vol%, with optimal trade-offs in heat transfer and pressure drop observed near 0.3 vol%. Turbulent regime enhancements ranged from 2.89 % to 14.63 %, with diminishing returns at higher concentrations. To further augment convective performance, externally applied magnetic fields with sine, square, and triangular waveforms were introduced. Among them, square wave excitation yielded the highest thermal gain (up to 39.21 %), followed by triangular (38.13 %) and sine waves (35.5 %) in transitional flows. Magnetic modulation consistently improved heat transfer in both regimes, albeit with increased pressure loss. A Thermal Efficiency Index (TEI) analysis revealed values above unity across all test cases, indicating a net thermohydraulic benefit. Furthermore, an entropy generation assessment showed that waveform-induced mixing mitigated thermal and viscous irreversibilities, thereby enhancing overall thermodynamic efficiency. These findings highlight the potential of waveform-controlled magnetic fields to optimize nanofluid performance in regime-sensitive thermal applications

1. Introduction

The growing demand for compact, energy-efficient thermal systems has intensified the search for advanced heat transfer fluids capable of meeting the rising heat dissipation needs in electronics cooling, energy systems, and industrial applications. Conventional fluids such as water, ethylene glycol, and oils often fall short due to their limited thermal conductivity. To overcome this, researchers have explored the use of nanofluids fluids containing suspended nanoparticles which offer moderate improvements in heat transfer performance.

However, mono nanofluids are often constrained by single-parameter optimization and trade-offs between conductivity and viscosity. This limitation has led to the emergence of hybrid nanofluids (HNFs) and more recently, ternary hybrid nanofluids (THNFs), which combine three distinct nanoparticles to exploit their synergistic thermal and fluidic properties. These advanced fluids are being investigated for next-generation applications such as nuclear cooling, microelectronics, and magnetically assisted thermal systems.

In this context, the present study introduces a novel THNF formulation consisting of Fe_3O_4 (magnetite), Al_2O_3 (alumina), and multi-walled carbon nanotubes (MWCNTs) dispersed in deionized water. This specific combination is strategically designed to integrate magnetic tunability (from Fe_3O_4), chemical and colloidal stability (from Al_2O_3), and ultra-high thermal conductivity with enhanced phonon transport (from MWCNTs). Unlike previously reported binary or ternary nanofluids, this unique formulation enables multi-scale thermal transport

* Corresponding author. Department of Mechanical and Industrial Engineering Technology, University of Johannesburg, Private Bag, Johannesburg, 2092, South Africa.
** Corresponding author. Department of Mechanical and Aeronautical Engineering, University of Pretoria, Pretoria, Private Bag X20, Hatfield, 0028, South Africa.
E-mail addresses: vadogbeji@uj.ac.za (V.O. Adogbeji), mohsen.sharifpur@up.ac.za (M. Sharifpur).

https://doi.org/10.1016/j.ijthermalsci.2025.110275
Received 7 July 2025; Received in revised form 21 August 2025; Accepted 29 August 2025
Available online 13 September 2025
1290-0729/© 2025 The Authors. Published by Elsevier Masson SAS. This is an open access article under the CC BY license (http://creativecommons.org/licenses/by/4.0/).

Table 1
Summary of magnetic field application for thermal exchange enhancement in nanofluids: methods and Re ranges in the laminar regime.

Investigators	Nanofluids	Reynolds number range	Magnetic field (MF) application	Methods for enhancing heat transfer
Sun et al. (2020) [7]	Fe_3O_4/H_2O	400–2000	Permanent magnet, 0.0415, 0.00700 and 1.28T, 40 KHz	Increasing the magnet frequency and an alternative MF. Peak 32 % enhancement with 0.007T with 1.28 T MF gradient.
Tekir Mutlu. (2025) [8].	Fe_3O_4/H_2O Fe_3O_4 Cu/H_2O	172–400	0.46 T external MF in plate heat exchanger	Hybrid nanofluids improved heat exchanger effectiveness by up to 20 % without MF. MF reduced effectiveness (up to 15 %) and heat transfer (up to 8 %) due to increased viscosity, suppressed mixing, and Lorentz force effects
Fatih and Öztop (2024) [9]	Nanofluid with encapsulated phase change materials (PCMs)	$200 \leq Re \leq 1000$	Ha = 0–60; most effective without internal rotation	Rotating inner walls, sinusoidal wavy wall, encapsulated PCM, wave amplitude variation, frequency tuning, neural network modeling
Habiyaremye & Wainaina. (2024) [10]	Silver $/H_2O$ nanofluids	Varied	MF in convergent/divergent microchannels	Ha reduced velocity via Lorentz forces; Re increased velocity in divergent channels but decreased it in convergent ones.
Miri et al. (2023) [11],	MHD nanofluids	Increasing Re examined	External MF in forced convection scenarios	Higher Re, Eckert number, and nanoparticle volume fraction enhanced *Nu*; however, larger Ha reduced efficiency
Varkaneh et al. (2023) [12]	Fe_3O_4/H_2O	Not specified	600 G transverse MF in corrugated heat exchanger.	Significant boost in Nusselt number and friction factor due to MF-induced convection
Tekir et al. (2020) [13]	Fe_3O_4/H_2O	1122–2124	Alternating/constant magnet (B = 0 T, 2 T, 5 T and 15 Hz).	Reductions in magnetic field frequency resulted in a 13 % improved in thermal transport
Zheng et al. (2024) [14].	Fe_3O_4/H_2O	Not specified	Multiple MF configurations in plate heat exchanger	MF enhanced heat transfer significantly; without MF, performance was lower than distilled water
Mei et al. (2019) [15]	Fe_3O_4/H_2O	600–1100	Parallel magnetic induction intensity, B = 0.001,0.002 and 0.003 T	With more nanoparticle additions and MF intensities strength led to maximum resistance coefficient at B = 0.003T.
Hatami et al. (2017) [16]	Fe_3O_4/H_2O	100–500	Electrical magnetically powered, uniform MF ($dH/dx < 9.6 \times 10^7$ A/m).	Stronger magnetic fields and higher particle densities enhanced convective heat transfer by over 60 %.
Wang et al. (2019) [17]	Fe_3O_4/H_2O	0–1000	Round hollow permanent magnet (internal dia. 39 mm, external dia. 62 mm, thickness 10 mm).	With more nanoparticle additions and MF intensity which led to improved thermal transport 26.5 % and 54.5 %.
Aydin et al. (2022) [18]	*Ni*Fe_2O_3/H_2O water (up to 3 %)	Not flow-based (thermosyphon)	Low parallel MF using current-carrying solenoid.	Magnetic field improved thermal exchange, uniform temperature distribution, and heat transfer was impacted by nanoparticle volume.
Taskesen et al. (2023) [19]	Fe_3O_4/H_2O	1000–2300	Constant external MF in circular pipe	MF enhanced convective heat transfer up to 8.32 %; higher flow rates increased *Nu*; MF shown to be effective in thermal control.
Amani et al. (2017) [20]	Fe_3O_4/H_2O	100–1200	Constant magnet 200	With more nanoparticle additions and magnetic field strength enhanced heat transfer by up to 8.5 %.
Lee et al. (2021) [21]	Fe_3O_4/MWCT/H_2O/EG	1000–1600	MF intensity varied (0.0025, 0.005, and 0.0075 T).	CHT rates increased by 2.78 %–3.23 % with higher particle concentrations.
Lee et al. (2021) [21]	$Co - Zn - Fe_3O_4/H_2O$	1000–1600	750 Gauss MF intensity.	Heat exchange was improved by 2.64 % due to nanoparticle loading and MF application
Tekir et al. (2022) [22]	$Fe_3O_4 - Cu/H_2O$	994–2337	constant/alternative, B = 0.3T At a 90-degree angle to the flow direction	By increasing the magnet frequency and applying a steady MF, the peak CHT increased by 14 % compared to conditions without a magnetic field
Shahsavar et al. (2016) [23]	Fe_3O_4−CNTs/H_2O	548–2190	MF intensities were set at three levels: 0.003, 0.003, and 0.007 T.	HNFs showed a 62.7 % increase in *Nu* with higher particle density and MF strength.
Shi et al. (2019) [24]	Fe_3O_4−CNTs/H_2O	60–540	Electromagnets with varying rotation angles and magnetic strengths (0.001, 0.002, 0.004, and 0.008 T).	Magnetic field and particle concentration enhanced heat exchange by 12.2 %, with local heat exchange up by 30.2 %.
Javadpour et al. (2017) [25]	Cuo/CMC/ H_2O	500–2000	Five permanent magnets with 50 mT.	Magnetic field increased heat exchange, with a 22.6 % rise in drag coefficient at 1 % volume fraction.
Javadpour et al. (2018) [26]	Cuo/CMC/ H_2O	500–2000	Five permanent magnets with 50 mT.	13 % augmentation at 1 % concentration nanofluid with the MF.
Alsarraf et al. (2019) [27]	Fe_3O_4/MWCT/H_2O	500 to 2000	Three NdFeB magnets creating a 3D magnetic field.	Increased particle volume concentration led to a 52.54 % increase in *Nu* and a 2376.4 % rise in pressure drag
Sadeghinezhad et al. (2017) [28]	rGO/Fe_3O_4/DW		Five permanent magnets with 50 mT flux density.	Magnetic field increased heat exchange, with a 22.6 % rise in drag coefficient at 1 % volume fraction.

enhancement and magnetic field controllability.

In addition to material modification, external enhancement techniques, such as magnetic field application and surface modification, are gaining traction. Magnetic fields, in particular, introduce magnetohydrodynamic (MHD) effects that alter flow behavior via Lorentz forces, leading to enhanced mixing and disrupted thermal boundary layers [1]. For example, Ahmad et al. [2], showed that magnetic excitation promotes early turbulence transition and strengthens thermal performance through the generation of secondary flow structures. Similarly, El-Zahar et al. [3] demonstrated that localized magnetic fields improve thermal uniformity and heat transfer under mixed convection conditions.

These effects are particularly critical in the transition flow regime [4], a region between laminar and turbulent flow (Re = 2300–4000) where small disturbances can significantly amplify convective heat transfer. Most industrial thermal systems operate in or near this regime, making it both a challenge and an opportunity for performance enhancement transfer [5,6]. Controlled destabilization of flow via nanoparticle loading and magnetic excitation has shown promising

Table 2
Summary of MF application for Heat dissipation improvement in nanofluids: methods and Reynolds number ranges in the turbulent regime.

Investigators	Nanofluids	Reynolds number range	Magnetic field (MF) application	Methods for enhancing heat transfer
Ebaid et al. (2022) [29]	Fe_3O_4/H_2O	1000 to 6000	MF (F = 15:5, 30:3, 45:5) mT	Higher *Nu* under the influence of a magnetic field resulted in an increase in average CHT and *Nu*. The enhancements recorded were 23.9 %, 26.1 %, 31.3 %,13.1 %, 9.4 %, and 8.8 %, respectively.
Asker et al. (2016)	Fe_3O_4/H_2O	2900–9160	constant magnetic field. magnetic intensity of (0.1, 0.2, 0.3 T),	Enhancing particle volume fraction and magnetic field strength led to gains of 43.9 %, 44.3 %, and 46 %.
Karamallah et al. (2006) [30]	Fe_3O_4/H_2O	2900 to 9820	a magnetic intensity of 0.1, 0.2, or 0.3 T	The improvements varied between 5.4 % and 42.7 %. However, with the application of a MF at intensities of 0.1, 0.2, or 0.3 T, the Nusselt number showed a substantial rise, attaining values of 43.9 %, 44.3 %, and 46 % at a particle volumetric ratio of 0.9 %.
Guzei et al. (2017) [31]	Fe_3O_4/H_2O	1000–6000	Three fixed neodymium magnets with a strength of 0.3 T.	The growth in nanoparticle loading and the application of a MF resulted in a 35 % enhancement in heat transfer efficiency
Zhang and Zhang (2021) [32]	Fe_3O_4/H_2O	944 to 8413	Alternating magnetic fields with frequencies ranging from 0 to 100 Hz and magnetic field intensities varying from 0.01 T to 0.09 T.	An externally applied oscillating magnetic field boosted heat exchange at lower Reynolds numbers but had an adverse effect at higher Reynolds numbers. Increasing both the nanoparticle concentration and MF frequency led to a higher pressure drop; however, once the volume fraction exceeded 3 %, further increases in frequency had a negligible effect on thermal exchange. Overall, thermal performance was enhanced between the 0–100 Hz of alternating MF.

results in promoting turbulence and increasing heat transfer rates.

To exploit the complementary properties of multiple nanoparticles, this study formulates a novel ternary hybrid nanofluid (THNF) composed of Fe_3O_4 , Al_2O_3 ,and MWCNTs dispersed in deionized water. This specific combination is strategically selected to maximize thermophysical synergy: Fe_3O_4 imparts magnetic responsiveness and moderate thermal conductivity; Al_2O_3 ensures chemical stability, dispersion reliability, and surface interaction; while MWCNTs contribute ultrahigh thermal conductivity and anisotropic heat transport due to their high aspect ratio. Unlike existing ternary mixtures that often rely on combinations of metal oxides or metallic particles alone, the inclusion of carbon-based MWCNTs introduces a unique thermal bridging mechanism, enhancing phonon transport and reducing interfacial resistance.

Compared to binary nanofluids, this tailored Fe_3O_4 –Al_2O_3–MWCNT formulation leverages a three-fold enhancement mechanism: magnetic field sensitivity (Fe_3O_4), enhanced surface stability (Al_2O_3), and superior conductive pathways (MWCNTs). This ternary synergy results in more efficient and controllable heat transfer behavior, especially under the influence of dynamic magnetic fields. Furthermore, while prior studies have largely focused on laminar or turbulent regimes, this work uniquely targets the underexplored transitional regime, incorporating the effects of waveform-controlled magnetic fields (sine, square, triangular), thereby revealing nonlinear enhancements in convective performance, entropy generation, and thermodynamic efficiency. These aspects mark a distinct advancement over previously reported binary or ternary nanofluid configurations

Ternary hybrid nanofluids (THNFs) offer significant advantages over conventional and hybrid nanofluids owing to their excellent thermal conductivity and heat dissipation characteristics [2]. These enhanced properties make THNFs highly effective in improving cooling efficiency and overall energy performance across various applications, including electric ovens, microfluidic devices, and nuclear reactors. However, the efficiency of THNFs is impacted by multiple factors, such as concentration, shape, nanoparticle selection, and size, along with the choice of primary fluid.

Tables 1 and 2 outline the evolution of research in nanofluids, starting with single-nanofluid approaches in laminar flow and progressing to more complex hybrid systems in turbulent regimes. The methods have increasingly focused on optimizing nanoparticle concentration, dispersion, and the synergistic effects of MF to maximize thermal transport efficiency. This summary highlights how different studies have applied Magnetically induced convection to boost heat dissipation in nanofluids, particularly across varying Reynolds number ranges and magnetic field applications. Common methods for enhancing heat transfer included adjusting nanoparticle content, magnetic field intensity, and frequency.

Despite the substantial advancements in nanofluid technology for convective heat transfer enhancement, most research efforts have primarily focused on mono and binary nanofluids, especially under laminar flow conditions. These studies, while foundational, often fall short in addressing the complexities and instabilities present in higher Reynolds number regimes such as the transition and turbulent regions where practical thermal systems like heat exchangers and cooling loops often operate.

Ternary nanofluids (THNFs), comprising three different types of nanoparticles, offer a promising yet underexplored path for further improving thermal conductivity, specific heat capacity, and suspension stability due to the synergistic effects between metallic, metal oxide, and carbon-based additives. In particular, the Fe_3O_4–Al_2O_3–MWCNT/water THNF used in this study combines magnetic responsiveness, high thermal conductivity, and strong dispersion characteristics making it highly suitable for applications requiring tunable thermal performance under dynamic conditions.

Moreover, the role of magnetohydrodynamic (MHD) effects in manipulating convective flow patterns has seen growing interest. However, prior studies have largely applied static or unidirectional magnetic fields, often neglecting the potential of oscillating magnetic fields with distinct waveform shapes (sine, square, triangular) to dynamically alter flow structures, suppress entropy generation, and enhance thermal transport.

This study is original in that it.

- Integrates a ternary hybrid nanofluid (Fe_3O_4–Al_2O_3–MWCNT) under oscillating magnetic field excitation, which has not been systematically studied, especially in the transition flow regime, where unsteady flow dynamics present unique challenges and opportunities.
- Introduces a comparative framework that evaluates how different waveform excitations impact heat transfer, pressure drop, and entropy generation offering a novel angle to optimize thermofluid performance in real-world scenarios.
- Links THNF formulation directly to convective heat transfer enhancement, not only through static property improvements but

also through dynamic field interaction, making the approach relevant for smart cooling systems, energy-efficient heat exchangers, and magnetically controlled microchannel flows.

By addressing the coupled effects of flow regime, nanoparticle hybridization, and magnetic waveform dynamics, this work contributes original insights that can guide the development of next-generation thermal-fluid technologies.

2. Experimental procedure

2.1. Synthesis of nanofluids and selection of materials

In this study, a combination of 15 % Fe_3O_4, 80 % Al_2O_3 and 5 % MWCNT nanoparticles was dispersed in deionized water using a two-step synthesis approach, resulting in volumetric ratio 0.0025 vol% to 0.3 vol%.

The selection of the hybridization mixing ratios 15 % Fe_3O_4, 80 % Al_2O_3, and 5 % MWCNT was based on a combination of literature support, thermophysical performance expectations, and engineering judgment. Specifically, Al_2O_3 was selected as the dominant component due to its known chemical stability, availability, and favorable thermal conductivity-to-cost ratio. A smaller proportion of Fe_3O_4 (15 %) was included to introduce magnetic responsiveness without excessive agglomeration or density-induced sedimentation. The MWCNT fraction (5 %) was deliberately kept low due to its high aspect ratio and strong influence on viscosity and thermal conductivity even at small loadings. This composition reflects a balanced trade-off among thermal conductivity enhancement, colloidal stability, and manageable viscosity consistent with prior hybrid nanofluid studies. The ratios were not the result of numerical optimization but were carefully selected based on trends reported in similar multi-component systems and our preliminary experimental screening

The thermodynamic and rheological properties of both the nanoparticles and the base fluid, as outlined in Table 3, were analysed for heat transfer experiments. To achieve uniform dispersion, the nanoparticles were initially mixed using a mechanically driven stirrer, followed by ultrasonication at 100 % amplitude for 4 h. The ultrasonication process was carried out in a temperature-controlled bath maintained at 20 °C. To enhance stability, Gum Arabic was introduced as a surfactant at a weight ratio of 0.5 %. The volume concentrations of the nanofluids were determined using Equations (1) and (2) [33,34]. A visual representation of the process is provided in Fig. 1.

Physical characterization, including viscosity measurements and stability assessments, was conducted over time at a constant temperature of 25 °C, with observations extending up to 12 h and one month. Stability evaluations involved both visual inspections and structured tests, with Fig. 1 depicting key aspects: (a) Step-by-Step Illustration of THNF Preparation and (b) a comparative visualization of nanofluid stability 24 h after synthesis. This meticulous preparation and evaluation framework ensures a comprehensive assessment of nanofluid performance and long-term stability across all samples.

$$\varphi = \left(\frac{Y_{Fe_3O_4}\left(\frac{W}{\rho}\right)_{Fe_3O_4} + Y_{Al_2O_3}\left(\frac{W}{\rho}\right)_{Al_2O_3} + Y_{MWCNT}\left(\frac{W}{\rho}\right)_{MWCNT}}{Y_{Fe_3O_4}\left(\frac{W}{\rho}\right)_{Fe_3O_4} + Y_{Al_2O_3}\left(\frac{W}{\rho}\right)_{Al_2O_3} + Y_{MWCNT}\left(\frac{W}{\rho}\right)_{MWCNT} + \left(\frac{W}{\rho}\right)_{DIW}} \right) \quad (1)$$

$$\rho_{Fe_3O_4/Al_2O_3/MWCNT} = \frac{\left(\rho_{Fe_3O_4} \times W_{Fe_3O_4}\right) + \left(\rho_{Al_2O_3} \times W_{Al_2O_3}\right) + \left(\rho_{MWCNT} \times W_{MWCNT}\right)}{W_{Fe_3O_4} + W_{Al_2O_3} + W_{MWCNT}} \quad (2)$$

where the nanoparticle type ratio of each is depicted by Y and W nanoparticle mass.

A range of instruments and analytical tools were utilized to perform specific measurements and analyses throughout the research, as outlined in Table 4.

2.2. Nanofluid sample preparation and stability testing via UV–vis spectrophotometry

The samples were analysed with a UV–visible spectrophotometer (Thermo Scientific Multiskan Go) at 24.8 °C, using distilled water as a reference (Fig. 2a). Six measurements were taken for each sample, and the averages were used for analysis. Sedimentation percentages were determined using Equation (3) [35,36],which quantifies the percentage of sedimentation in the nanofluids.

The spectrum was scanned from 200 to 1000 nm, with 100 nm intervals from 200 to 700 nm and 50 nm intervals from 750 to 1000 nm.

Table 3
Thermophysical properties of the investigated materials at ambient temperature.

Thermophysical properties	Nanoparticle	Manufacturers Value	Particle size (nm)	Manufacturers	Purity	Morphology
Dispersant Gum Arabic	Gum Arabic			Sigma-Aldrich, Germany		
Specific heat (J/kg.K)	Fe_3O_4	670				
	Al_2O_3	765				
	MWCNT	711				
	DIW	4179				
Thermal conductivity (W/m.K)	Fe_3O_4	80.4	(20–30 nm)	Nanostructured and Amorphous Material Inc., USA	99 %	Plate-like nanosheet
Density (kg/m^3)	Al_2O_3	37	(20–30 nm)		99 %	Spherical
	MWCNT	3000	(7 nm)		>95	
	DIW	0.613				
	DIW	997				

Reference: Material specifications provided by Nano Research Materials Inc. (USA) (US4314).

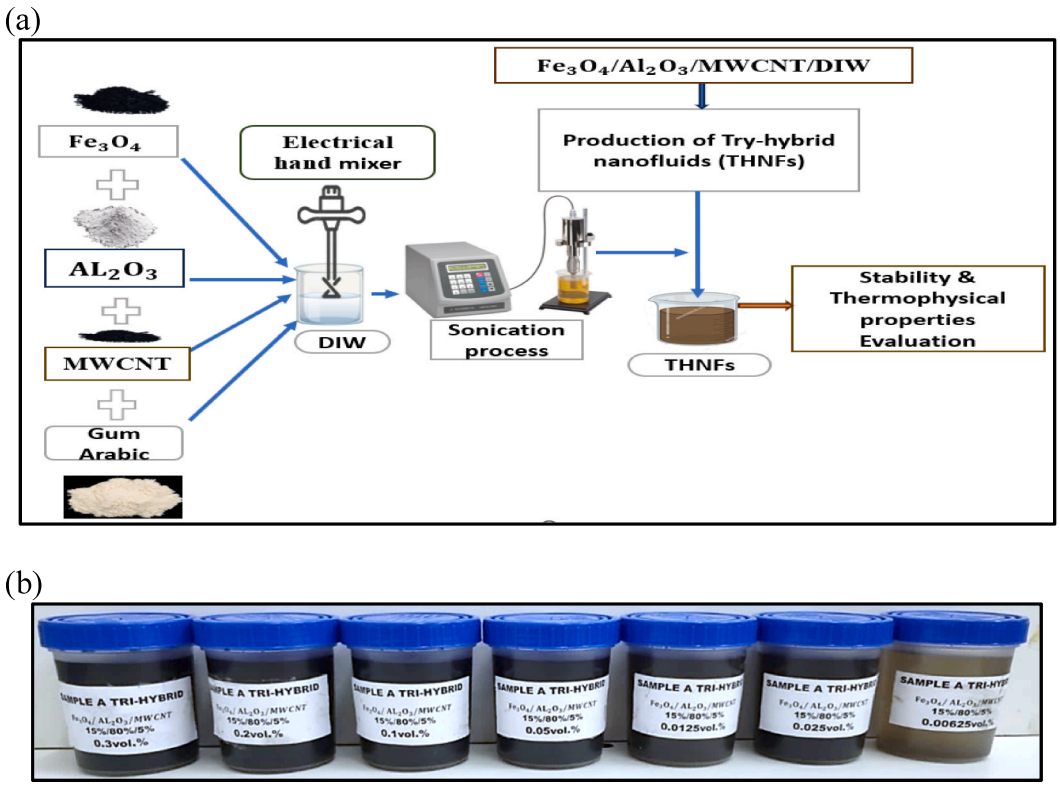


Figure:1. (a) Step-by-Step Illustration of THNF Preparation (b) a comparative visualization of nanofluid stability after 24 h post-preparation for all samples.

Table 4
Overview of analytical and measurement tools used.

Equipment/Instrument	Model/Manufacturer	Purpose	Specifications/Accuracy
Conductivity Meter	CHAUVIN ARNOUX, C.A 10141, France	Measuring electrical conductivity of MHNFs	Accuracy: ±1 %
Scanning Electron Microscopy (SEM),	JEOL JEM-2100F, Tokyo, Japan	Examining nanoparticle morphology in dry state	Not specified
Temperature Range for Tests	–	Thermal conductivity and viscosity measurements	10 °C–50 °C
UV–Visible Spectrophotometer	Thermo Scientific Multiskan Go Spectrophotometer	Determining absorbance and sedimentation	Not specified
pH Meter	Jenway 3510, Staffordshire, UK	Measuring pH levels of nanofluid samples	Range: −2 to 19.999; Accuracy: ±0.003
Vibro-Viscometer	SV-10A series, A&D, Tokyo, Japan	Measuring viscosity of MHNFs	Accuracy: ±1 %
Thermal Conductivity Analyzer	KD2 Pro, Decagon Devices Inc (METER Group)	Measuring thermal conductivity (κ) of MHNFs	Range: 0.02–2.0 kW/m^2 Accuracy: ±10 %

Absorbance measurements across these ranges allowed for the assessment of stability and dispersion quality. The sedimentation percentage, calculated from absorbance values, provided insights into the prolonged stability of nanofluids, vital for their thermal applications.

$$\text{Sedimentation factor (SF)} = \left(\frac{\textit{Maximum absorbance} - \textit{Total average absorbance}}{\text{Maximum absorbance}}\right) \times 100 \quad (3)$$

2.3. SEM analysis and XRD characterization procedures

For SEM imaging, aluminum stubs were used as sample holders with carbon tape applied to secure the nanoparticles. The particles were evenly distributed on the tape, and the stubs were then transferred to a Quorum Q1556 S/E/ES carbon coater (see Fig. 2b), where a thin carbon layer was deposited to improve conductivity. Once coated, the samples were loaded into the Zeiss Crossbeam 540 FEG-SEM (see Fig. 2c), mounted on the microscope stage, and the vacuum system was activated. The focus was carefully adjusted to obtain sharp, undistorted images. This process was repeated until clear images were captured at magnifications of 20k, 50k, and 100k, allowing for detailed examination of the nanoparticle morphology.

For XRD characterization, the structural properties of Al_2O_3, MWCNT, and Fe_3O_4 nanoparticles were analysed using a D8 X-ray diffractometer (see Fig. 2d). The samples were ground in an agate mortar and pestle before being placed into a sample holder (1.5 cm in

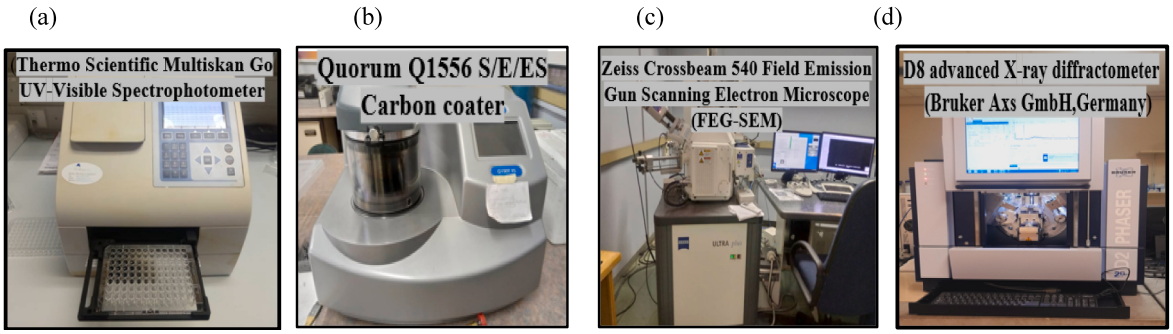


Fig. 2. Samples of equipment used (a) spectrophotometry (b) Carbon coater (c) SEM microscopy (d) X-ray diffractometer.

diameter and 1 mm thick) with a glass plate to ensure a flat surface. The samples were positioned in the path of the X-ray beam, and the stage was rotated for uniform exposure. A V20 slit controlled the divergence of the beam before it reached the sample. With an X-ray source of CuKα (1.54056 Å), the diffracted radiation was recorded by the detector. The experiment was conducted at a tube voltage of 40 kV and a current of 40 mA, with a scanning rate of 2° per minute over a 25°–60° range at room temperature. The diffraction data were subsequently processed using Origin software.

2.4. Measurement of thermal and physical properties (thermal conductivity (TC), pH, electrical conductivity (EC), and viscosity (μ)

The estimation of TC, pH, EC, and viscosity is essential for evaluating the efficiency and stability of nanofluids in heat transfer systems. TC defines a fluid's heat transfer ability, directly influencing cooling performance. Viscosity (μ) affects flow dynamics and pumping power, where high viscosity increases friction and reduces efficiency. Density impacts mass flow rates and pressure drops, crucial for system design. EC reflects the fluid's charge-carrying capacity, which can improve nanoparticle dispersion and allow for electromagnetic control in heat transfer applications. pH stability is vital to prevent nanoparticle agglomeration and ensure consistent thermal performance. Proper measurement of these properties aids in optimizing nanofluid formulations, boosting heat transfer efficiency and system reliability.

2.4.1. Thermal conductivity measurements (TC)

Before initiating the measurements, the thermal conductivity instrument was first calibrated using a standard fluid (glycerine) with known thermal properties. After calibration, the thermal conductivity of deionized water was recorded across a temperature range of 10 °C–50 °C, and these results were In contrast to the benchmark values provided by Yunus & Ghajar [37]. Following this, the TC of the Fe_3O_4/Al_2O_3/MWCNT-DIW thermal nanofluids was evaluated over the same temperature span. Each test was conducted six times, with the average value from these repetitions being used for further analysis.

For these experiments, a KD2 Pro thermal properties measurement system from Decagon Devices Inc. (USA) was employed. This system is capable of measuring TC in the range of 0.02 W m^{-1} K^{-1} to 2 W m^{-1} K^{-1} and carries an uncertainty of 5 % as specified by the manufacturer. To achieve accurate results, it was necessary to align at least 15 mm of the sample aligned with the sensor in every direction, since the sensor releases a heat pulse during the measurement process. The thermal nanofluid samples, labelled from 0.0025 vol% to 0.0025 vol%, correspond to various nanoparticle volume fractions. The KD2 Pro system, which applies the transient hot-wire approach, involving of a handheld controller and a series of sensor needles. The specific sensor needle used in these experiments has an accuracy of 5 % for the TC measurements of the nanofluids.

Finally, the enhancement in thermal conductivity for the thermal nanofluids was calculated using Equation (4).

$$\%_{improvement} = \left(\frac{K_{nf} - K_{bf}}{K_{bf}}\right) \times 100 \quad (4)$$

2.4.2. Evaluation of electrical conductivity and pH of THNFs

The EC instrument was first adjusted using a manufacturer-supplied standard fluid. At 25 °C, the calibration fluid was measured three times, resulting in an average conductivity of 1413.6 μS cm^{-1}. Following calibration, the electrical conductivity of both deionized water and the ternary nanofluid samples was recorded over a temperature span of 10 °C–50 °C at 5 °C intervals. The increment in conductivity for the nanofluids was estimated with Equation (5).

Similarly, the pH meter was set up with buffer solutions of pH 4, 7, and 10. Once calibrated, the pH of the hybrid nanofluid samples was measured, as shown in Fig. 3.

$$\%_{improvement} = \left(\frac{EC_{nf} - EC_{bf}}{EC_{bf}}\right) \times 100 \quad (5)$$

2.4.3. Measurement of viscosity (μ)

Before assessing the μ of deionized water and Fe_3O_4/Al_2O_3/MWCNT-DIW thermal nanofluids across the 10 °C–50 °C range, the vibration-based viscosity meter (SV-10A series, A&D, Tokyo, Japan) was calibrated. A 1.1 % discrepancy was evident when assessing the measured viscosity of deionized H_2O with its standard value.

To maintain consistent thermal conditions during the experiment, the setup was connected to a programmable thermal control system (LAUDA, Berlin, Germany, model ECO RE1225) and integrated with a data recording device, as shown in Fig. 3c. The collected data were subsequently processed and analysed. The enhancement in viscosity for the thermal nanofluids was calculated using Equation 6

$$\%_{improvement} = \left(\frac{\mu_{nf} - \mu_{bf}}{\mu_{bf}}\right) \times 100 \quad (6)$$

2.5. Nanoparticle composition and structural analysis (n_p)

A thorough structural investigation of Fe_3O_4, Al_2O_3, and MWCNT n_p was examined using a Zeiss Crossbeam 540 FEG-SEM, located at the Microscopy Department of the University of Pretoria. To ensure the best possible imaging results, the samples were carefully prepared before analysis. The micrographs, shown in Fig. 4, illustrate that Fe_3O_4 nanoparticles have a spherical shape with distinct clustering patterns, while Al_2O_3 nanoparticles are observed as tightly packed spheres. In contrast, the MWCNT nanoparticles maintain a uniform cylindrical shape, resembling interconnected chains with some signs of aggregation.

The micrograph of the Fe_3O_4/ Al_2O_3/MWCNT/ n_p reveals that Al_2O_3 particles tend to attach to the edges of the aggregated, blade-like Fe_3O_4 particles and the chain-like MWCNTs, forming a complex composite structure. This arrangement could potentially enhance thermophoretic forces when the nanoparticles are dispersed in a liquid, possibly

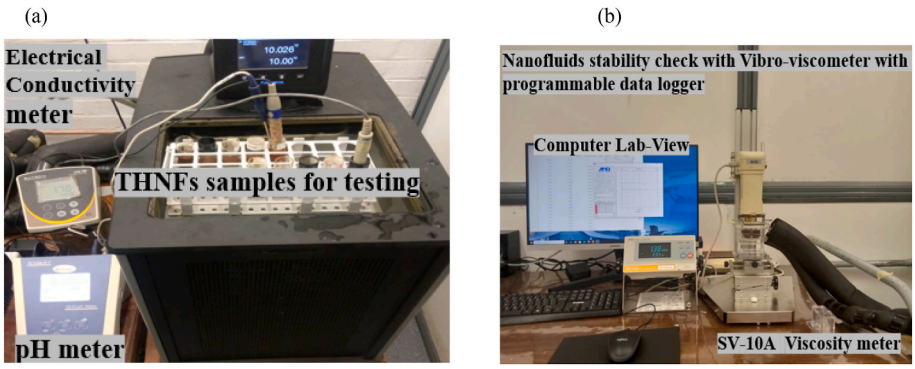


Fig. 3. Measurement equipment used: (a) pH and Electrical meter with thermal bath (b) SV-10A Vibro-viscometer with Data logger.

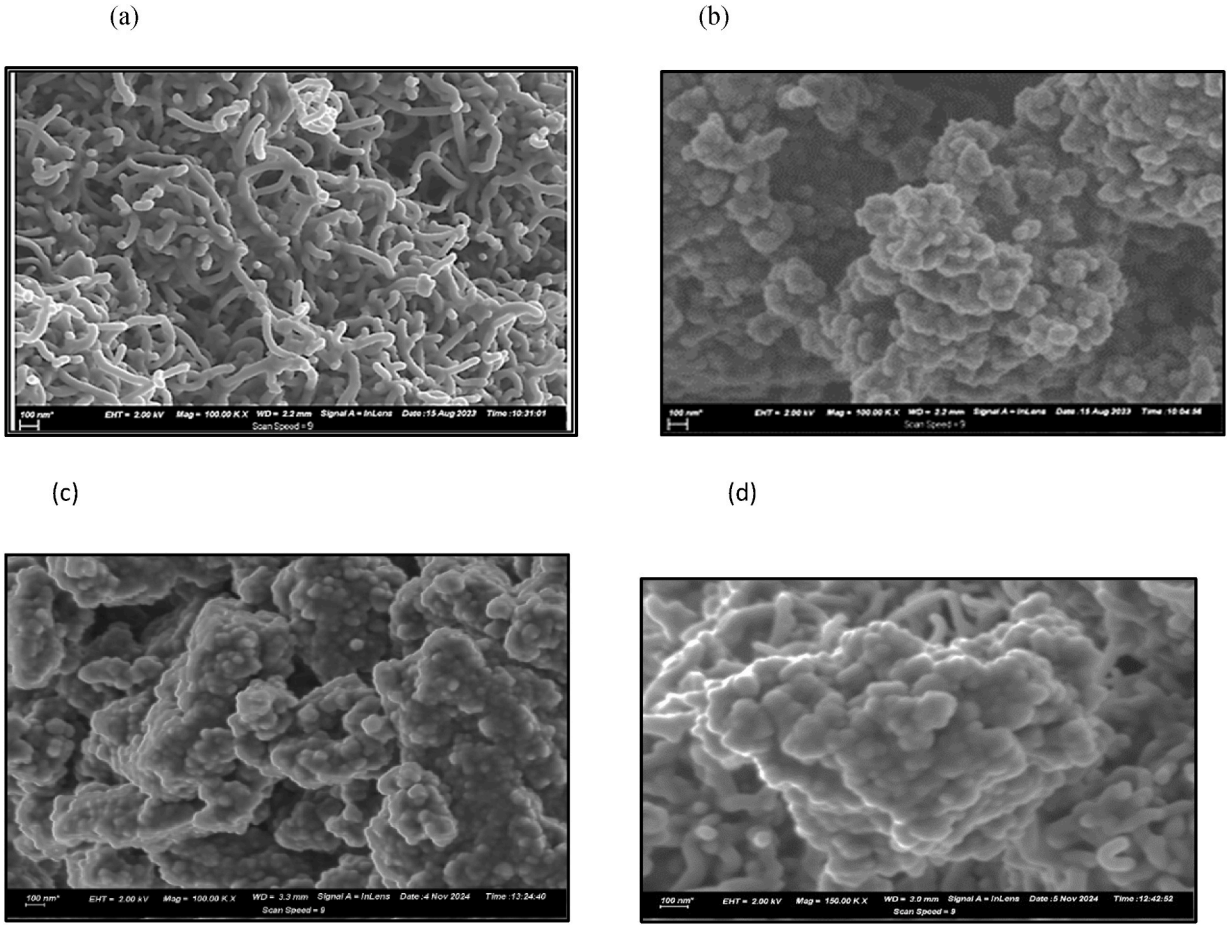


Fig. 4. Structural features of nanoparticles (a) MWCNT (b) Al_2O_3 (c) Fe_3O_4 (d) Fe_3O_4/ Al_2O_3/MWCNT at magnification of 100KX.

improving their electro- and thermophoretic behaviors under thermal and electrical conditions. These findings align with earlier research on nanoparticle morphology, further confirming the accuracy of the nanoparticles' characterization as provided by the manufacturers.

2.6. X-ray diffraction (XRD) analysis for structural characterization of MWCNT, Fe_3O_4*,and* Al_2O_3*. Nanoparticles*

X-ray diffraction (XRD) was employed to examine the crystalline behaviours of the ternary nanoparticles (MWCNT, Fe_3O_4,and Al_2O_3). In Fig. 5a, the diffraction pattern of the MWCNTs displays distinct peaks at 25.96° and 43.1°, which are attributed to the (002) and (100) planes, respectively. The dominant (002) reflection confirms the presence of a well-ordered graphite lattice within the carbon nanotubes. Additionally, the lattice parameters were determined to be a = b = 2.47 Å and c = 6.79 Å, indicative of a hexagonal structure that falls within the $P6_3mc$ space group. These results are in strong agreement with the reference data from JCPDS card No. 96-101-1061, and the average crystallite size was calculated to be 16.7 nm, consistent with earlier reports such as those by khedaer et al. [38].

For the Fe_3O_4 nanoparticles shown in Fig. 5b, the diffraction peaks appear at 2θ angles of 30.1°, 35.4°, 43.1°, 53.7°, 56.9°, 62.8°, and 74.5°. These peaks correspond to the (220), (311), (400), (422), (511), (440), and (533) planes, which are characteristic of the cubic inverse spinel structure of magnetite. This pattern aligns well with the data provided by JCPDS card No. 19–0629.

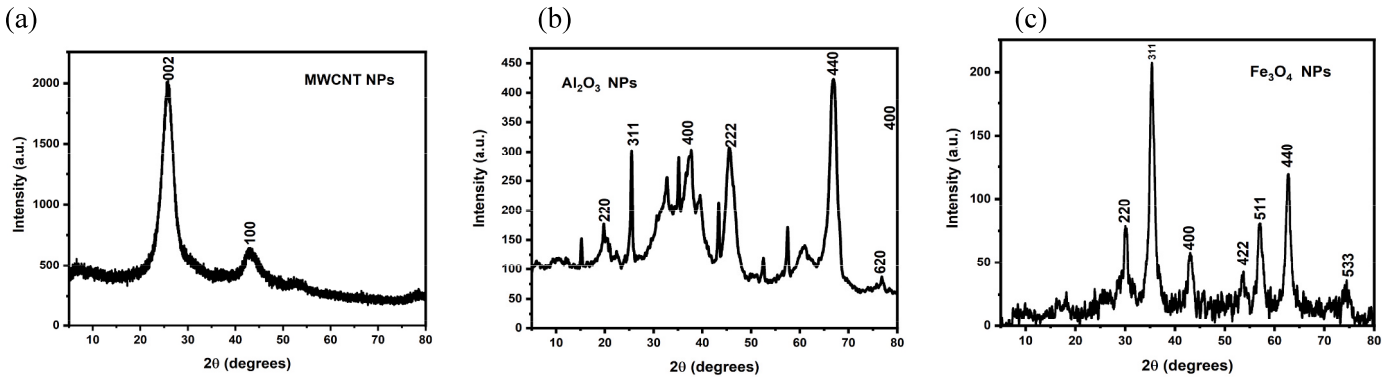


Fig. 5. Ternary nanoparticles,(a) MWCNT NPs, (b) Fe_3O_4 NPs, and (c) Al_2O_3 NPs.

Similarly, Fig. 5c presents the XRD profile for Al_2O_3 nanoparticles, where peaks at approximately 25.6°, 35.1°, 37.8°, 43.3°, 52.6°, 57.5°, 61.1°, 67.1°, and 77.1° have been recorded. These reflections are indexed to the (012), (104), (110), (113), (024), (116), (122), (214), and (119) planes, verifying the hexagonal crystal structure with an R-3c space group, as per ICDD card No. 00-010-0173. Some extra peaks in the diffraction data suggest the presence of minor impurities. The crystallite sizes for these nanoparticles were determined using the Debye-Scherrer equation (Equation (9)) as described in Refs. [39,40].

$$D = \frac{K\lambda}{\beta \cos\theta} \tag{7}$$

where θ represents the Bragg diffraction angle in radians, λ is the X-ray wavelength (λ = 1.5406 Å), β is the full width at half maximum (FWHM) in radians, κ is the Scherrer constant (typically 0.9), and D is the average crystallite size. Based on these calculations, the average crystallite sizes for MWCNT, Fe_3O_4, and Al_2O_3 were found to be 31.9 nm, 14.8 nm, and 25.7 nm, respectively. These values are consistent with those reported by Zhuang et al. [41], and Mohammed et al. [42] for similar nanoparticles.

2.7. *Assessment of stability* Fe_3O_4/ Al_2O_3*/MWCNT/DIW nanofluids and thermophysical properties*

To evaluate the stability of Fe_3O_4/ Al_2O_3/MWCNT/DIW nanofluids at different volume ratios, ultraviolet–visible (UV–Vis) spectrophotometry was employed, following methodologies outlined in previous research [43,44], The stability of the nanofluid (THNF) samples was assessed using a UV–visible spectrophotometer (Thermo Scientific Multiskan Go) under controlled ambient conditions (24.8 °C). Distilled water was employed as the baseline reference. To ensure measurement reliability, each sample was tested six times, and the average of these readings was used for subsequent analysis. The sedimentation percentage was determined using Equation (3) [35], which quantifies sediment accumulation in the nanofluids.

Spectral analysis was conducted over a wide wavelength range of 200–1000 nm. A scanning interval of 100 nm was applied from 200 to 700 nm, while a finer interval of 50 nm was used between 750 and 1000 nm to achieve a more detailed spectral resolution. This absorbance data across varying wavelengths provided valuable insights into the dispersion uniformity and colloidal stability of the THNFs.

By analyzing the absorbance trends across the selected wavelengths, sedimentation rates were derived, offering a quantitative measure of the nanofluid's dispersion integrity over time. This approach supports a comprehensive evaluation of particle stability and agglomeration behavior, which are critical for determining the feasibility and durability of THNFs in thermal management applications. The calculated sedimentation factor serves as a key parameter reflecting the long-term stability and effectiveness of the nanofluid system.

Fig. 6a illustrate the correlation between the absorption characteristics and composition of the nanofluids. A primary challenge in working with nanofluids is the tendency of nanoparticles to cluster due to strong van der Waals forces, which dominate the weaker repulsive interactions between particles, particularly when intensified by Brownian motion [45]. This aggregation increases particle density relative to the base fluid and can contribute to the formation of crystalline structures [33]. The phenomenon, commonly referred to as "particle agglomeration," negatively impacts the prolonged stability of nanofluids of the nanofluid, making stability a vital factor for thermal applications.

Sedimentation analysis is widely recognized as a reliable technique for assessing nanofluid stability. The principle behind this method involves observing the rate at which particles settle at the bottom of a container due to gravitational forces. A more stable nanofluid takes longer to exhibit visible sedimentation. Previous studies by Chakraborty et al. [46,47], and [48] have explored the use of sedimentation-based assessments for determining nanofluid stability. In this study, sedimentation tests were conducted on Fe_3O_4/ Al_2O_3/MWCNT/DIW nanofluids with different hybrid compositions to further examine their dispersion characteristics.

A key parameter in these stability evaluations is the sedimentation factor (SF). A higher SF percentage signifies superior nanoparticle dispersion and prolonged stability, with minimal particle settling over time. Conversely, lower SF percentages indicate a higher rate of sedimentation due to increased nanoparticle aggregation, resulting in diminished long-term stability.

Each tested nanofluid sample contained varying weight proportions of Fe_3O_4, Al_2O_3 and MWCNT, influencing both their dispersion properties and thermophysical behavior. The SF values were measured across volume fractions 0.3 %–0.00625 %, and the findings are summarized in Table 5 and Fig. 6a

The table presents sedimentation factor (SF) values for different nanofluid samples at varying concentrations. Higher SF values indicate better stability and reduced particle settling, while lower values suggest rapid sedimentation and weaker dispersion. Among the samples analysed, Sample A demonstrated the highest stability across all tested concentrations, whereas Sample E exhibited the lowest SF values, signifying faster nanoparticle deposition.

For the THNFs (15 wt% Fe_3O_4, 80 wt% Al_2O_3, 5 wt% MWCNT), the highest SF of 89.56 % was observed at 0.00625 % volume fraction, demonstrating superior stability at lower concentrations. As the volume fraction increased to 0.3 %, the SF dropped significantly to 12.39 %, indicating higher sedimentation and reduced stability at higher nanoparticle concentrations.

For the THNFs (15 wt% Fe_3O_4, 80 wt% Al_2O_3, 5 wt% MWCNT), the maximum SF of 89.56 % was recorded at a 0.00625 % volumetric ratio, indicating enhanced stability at lower volumetric. However, as the volume fraction increased to 0.3 %, the SF drastically declined to 12.39 %, suggesting greater particle sedimentation and diminished stability at

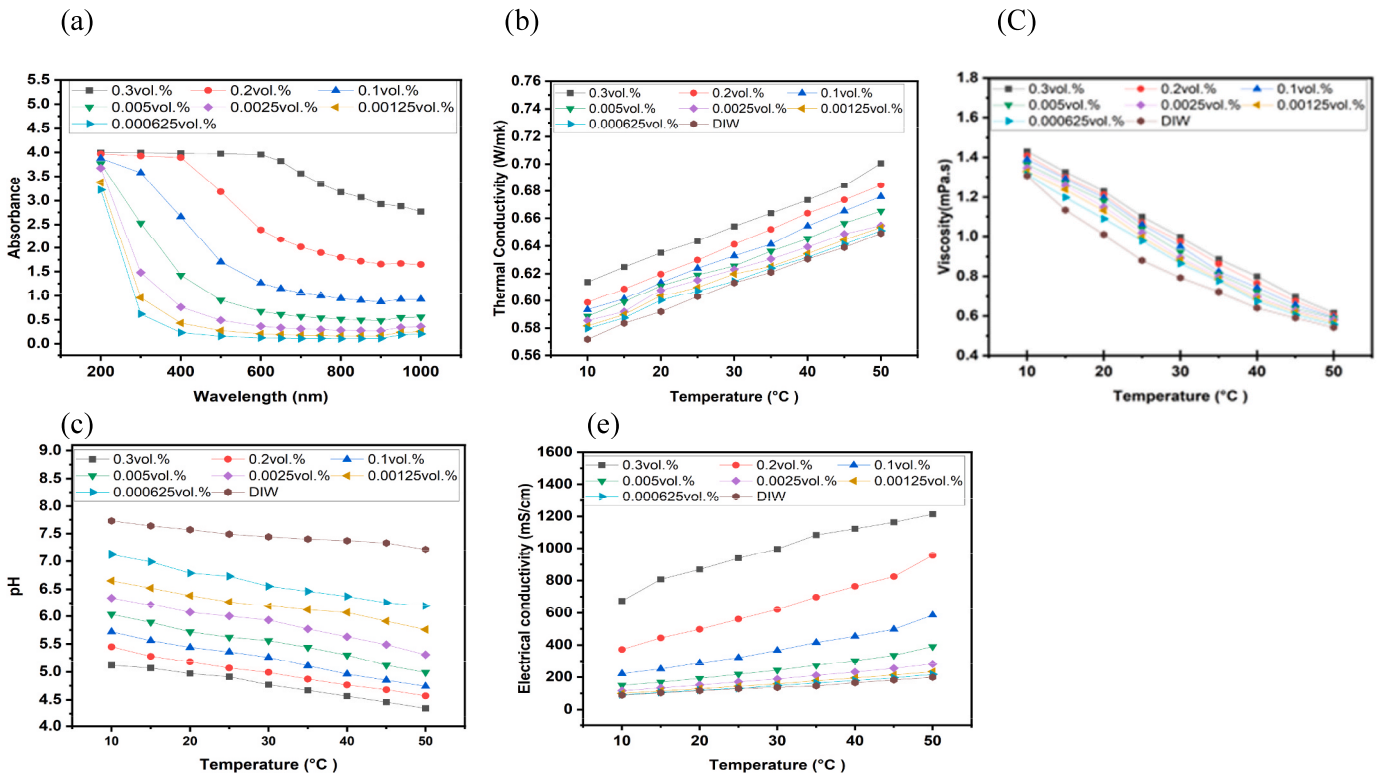


Fig. 6. Influence on the Thermo-Physical Behavior of THNFs (a) The stability of **Fe_3O_4/ Al_2O_3**/MWCNT/DIW with (UV–Vis) spectrophotometry (b) TC against temperature (c) viscosity against temperature (d) pH against temperature (e) EC against temperature.

Table 5
Sedimentation factor (SF) for nanofluid samples A at varying volume fractions.

	Sedimentation Factor						
Samples/vol%	0.3	0.2	0.1	0.05	0.025	0.0125	0.00625
A	12.392	38.431	59.775	73.736	82.165	86.921	89.562

higher concentrations.

These findings highlight that nanofluids maintain better dispersion at lower volume fractions, where SF values remain high, confirming minimal nanoparticle aggregation. Conversely, increasing nanoparticle concentration intensifies interparticle attractions, leading to clustering and a decrease in SF, thereby reducing stability. Among the tested volume fractions, 0.00625 % exhibited the most stable dispersion, reinforcing that the Fe_3O_4 and MWCNT ratios significantly affect sedimentation characteristics.

Moreover, enhancing thermal systems does not necessarily require a higher nanoparticle loading, as increased concentrations can elevate energy demands and contribute to clogging within fluid channels. These observations align with previous studies on Fe_3O_4-based hybrid nanofluids, including Fe_3O_4/TiO_2, Fe_3O_4/MgO, Fe_3O_4/ZnO, and Fe_3O_4/MWCNT combinations. In those studies, smaller nanoparticle concentrations (0.0125 % and 0.00625 %) demonstrated superior thermal transport performance while minimizing pressure drop concerns. This further confirms that 0.0125 % and 0.00625 % represent optimal concentrations for maximizing thermal efficiency without imposing additional flow resistance, as supported by prior research [4, 35,49].

Additionally, these results suggest that using lower nanoparticle concentrations reduces overall nanofluid production costs while maintaining excellent stability. The minimal settling observed at these optimal volume fractions enhances their practicality, reinforcing the potential of low-concentration nanofluids for cost-effective and efficient thermal management applications.

Fig. 6b presents the impact of varying volume fractions on the thermal conductivity (TC) THNFs in comparison to DIW. The study demonstrates that the ratio of Fe_3O_4, Al_2O_3, and MWCNTs is crucial for boosting heat transfer performance. Across the examined temperature range, TC exhibited a rising trend, with the nanofluid composition of 15 wt% Fe_3O_4, 80 wt% Al_2O_3, and 5 wt% MWCNTs showing a marked increase from 0.61391 W/m·K at 10 °C to 0.70052 W/m·K at 50 °C outperforming DIW. This improvement is attributed to Fe_3O_4's ability to facilitate magnetically induced heat transport, MWCNTs' superior thermal conductivity, and Al_2O_3's stabilizing effect. However, increasing nanoparticle loading influences both viscosity and sedimentation. This inverse relationship highlights the challenge of balancing enhanced TC with long-term suspension stability. The results suggest that while higher concentrations improve heat transfer efficiency, they also introduce undesirable effects, such as increased sedimentation and potential clogging. Sample A emerges as the most effective composition, offering an optimal balance between thermal performance and dispersion stability. The findings underscore the importance of using lower volume fractions to achieve an efficient and cost-effective thermal management solution while minimizing nanoparticle aggregation.

Fig. 6c illustrates how viscosity changes with temperature and volumetric fraction for all tested nanofluid samples compared to DIW. The rheological behavior of the hybrid nanofluid is shaped by the characteristic and interactions of Fe_3O_4, Al_2O_3, and MWCNTs. The inclusion of Fe_3O_4, which possesses magnetic properties, can lead to the formation of aligned structures in the presence of an external MF, causing a rise in viscosity. However, due to their spherical morphology,

Fe_3O_4 particles promote relatively smooth fluid motion compared to fibrous structures like MWCNTs. Al_2O_3 nanoparticles, characterized by their stability and high thermal conductivity, contribute minimally to viscosity changes as they tend to remain evenly dispersed without clustering. MWCNTs, with their high aspect ratio and strong tendency to interconnect, exert the most significant effect on viscosity, increasing resistance to flow. Temperature and volumetric play a critical role in viscosity variation, with higher temperatures generally reducing viscosity across all tested volume fraction. This viscosity behavior has important implications for practical applications: while increasing the nanoparticle concentration enhances thermal performance, it also results in greater viscosity, which could increase energy consumption in fluid circulation systems. Therefore, striking a balance between improving heat transfer and maintaining feasible viscosity levels is essential for optimizing performance.

As depicted in Fig. 6d, the pH behavior of nanofluids varies in response to both temperature shifts and volume fraction changes, with DIW serving as a comparative benchmark. The structural integrity and functional properties of nanofluids are highly dependent on these pH fluctuations. A rising temperature leads to a gradual pH decline, whereas lower nanoparticle concentrations result in an increase in pH. While DIW follows a similar pattern, its pH remains within a neutral range (7.73 at 10 °C to 7.21 at 50 °C), highlighting its chemical stability.

THNFS shows that the pH spans from 4.35 at 50 °C (0.03 vol%) to 6.19 at 50 °C (0.000625 vol%), as illustrated in Fig. 6d. The acidic properties of this nanofluid raise concerns regarding long-term material compatibility, particularly for metallic system components. However, its well-balanced dispersion contributes to efficient thermal conductivity. The presence of Fe_3O_4 further enables potential applications in magnetically controlled heat dissipation systems, making it a promising candidate for smart thermal regulation technologies.

The pH behavior of nanofluids is closely linked to the individual contributions of each nanoparticle type. Fe_3O_4 promotes a more acidic environment due to its tendency to oxidize and release iron ions, leading to a decrease in pH with increasing concentration. MWCNTs, while generally neutral, can introduce mild alkalinity due to their large surface area and surface modifications. Al_2O_3, on the other hand, has little direct impact on pH but enhances the dispersion stability of the nanofluid, which may help mitigate the acidity caused by Fe_3O_4

The balance between thermal enhancement and stability is evident in these findings. While higher concentrations of Fe_3O_4 and MWCNTs improve thermal transport properties, they also contribute to higher viscosity and faster sedimentation, which negatively affect stability. Additionally, the acidic nature of certain nanofluid compositions raises potential concerns about corrosion in metallic components, which could influence the long-term viability of these fluids in industrial thermal management applications.

Fig. 6e illustrates the trend of electrical conductivity (EC) variation concerning nanoparticle composition in Fe_3O_4/ Al_2O_3/MWCNT nanofluids under different temperature conditions. The EC of such nanofluids is significantly affected by both the type and concentration of nanoparticles dispersed in the base medium, which, in this case, is DIW.

The EC of nanofluids is a key parameter in thermal management, particularly when incorporating conductive nanoparticles like Fe_3O_4 and MWCNTs. Although EC does not directly correlate with heat transfer performance, it plays an essential role in applications related to cooling and thermal dissipation. As the nanoparticle concentration increases from 0.000625 vol% to 0.3 vol%, a clear enhancement in EC is observed. Additionally, the EC of the THNFs exhibits a linear increase with rising temperature, confirming that both volumetric fraction and temperature significantly influence conductivity.

These findings align with previous studies that demonstrated improvements in nanofluid EC due to temperature elevation, nanoparticle selection, and volume concentration [50–52]. The observed enhancement in EC compared to the base fluid across different temperature conditions further highlights the impact of nanoparticle incorporation on nanofluid electrical properties.

3. Experimental setup and methodology

To analyse CHT under a constant heat flux boundary condition, a custom experimental setup was designed and assembled. Fig. 7a and b depict the schematic layout, which includes a fluid circulation system comprising a flow meter, pump, heated test section, cooling unit, and storage reservoir.

The test section consists of a 1000 mm-long horizontal copper tube with an inner diameter of 8 mm and an outer diameter of 9.8 mm. A 500 mm segment is designated for achieving fully developed hydrodynamic flow before the fluid enters the heated section. A 200 W Constantan wire, powered by a direct current source operating at 1.22 A and 180 V, serves as the heating element at 219.8 W ($q \approx 8.67$ kW/m^2), ensuring a constant heat flux distribution along the pipe's upper surface [53].

To examine the impact of a MF on fluid flow and thermal exchange, four electromagnets were strategically positioned along the 1000 mm length of the copper tube. These electromagnets provide an adjustable magnetic field that can influence the movement and orientation of magnetic nanoparticles in the nanofluid, potentially altering its thermal and rheological properties.

To minimize heat loss, the setup is well insulated with 70 mm of insulating material, consisting of six layers of thermal protection. To monitor temperature variations along the test section, nine T-type thermocouples were strategically placed at axial distances from the inlet: (T1) 130 mm, (T2) 260 mm, (T3) 390 mm, (T4) 520 mm, (T5) 650 mm, (T6) 780 mm, and (T7) 910 mm. Additionally, two T-type temperature sensor were installed at the input and output to track fluid temperature changes.

A tube-in-tube heat exchanger was implemented to regulate the temperature of the working fluid and maintain a stable state thermal conditions. A constant-temperature bath was integrated into the cooling unit to regulate heat dissipation efficiently.

3.1. Setup, procedure, and measurement techniques

Following system startup, a stabilization period of at least 60 min given time to stabilize and ensure steady-state conditions. Stability was confirmed when fluctuations in pressure, temperature, and flow rate were negligible. Once equilibrium was established, flow rates were incrementally adjusted to achieve the required conditions. Each time the flow rate was modified, particularly when shifting from higher to lower values, the system required around 10 min to re-stabilize. To minimize residual heat effects on subsequent readings, measurements were carried out beginning with the highest flow rate and gradually reduced. For each condition, 200 data points were collected using a signal logger, and the average values were analysed.

3.2. Magnetic system configuration for optimized heat transfer in THNFs

This research adopts the approach outlined by Adogbeji et al. [46], where different voltage levels (2V, 4V, 6V, 8V, and 12V) and frequency variations (40 Hz–1000 Hz) were employed while maintaining a 50 % duty cycle and a phase shift of 90°. The study utilized sine, square, and triangular waveforms with corresponding cycle durations of 16.7 ms, 12.5 ms, 10.0 ms, and 20.0 ms to assess the impact of MF characteristics on fluid flow and thermal dissipation.

The experimental system comprised a UNIT UT900E Function Generator, magnetic coils (220L × 46W × 29D),a Digital Oscilloscope (IDS-2000A), a GM08 Magnetic Field Meter and a TS250 Signal Amplifier, and. The coils, powered by a 12V or 24V DC source (maximum 250 mA), were energized through the amplifier, which also controlled the waveform type and frequency. Four magnetic coils were arranged above the test section, covering all seven temperature sensor locations. Before activating the field under uniform heat flux conditions,

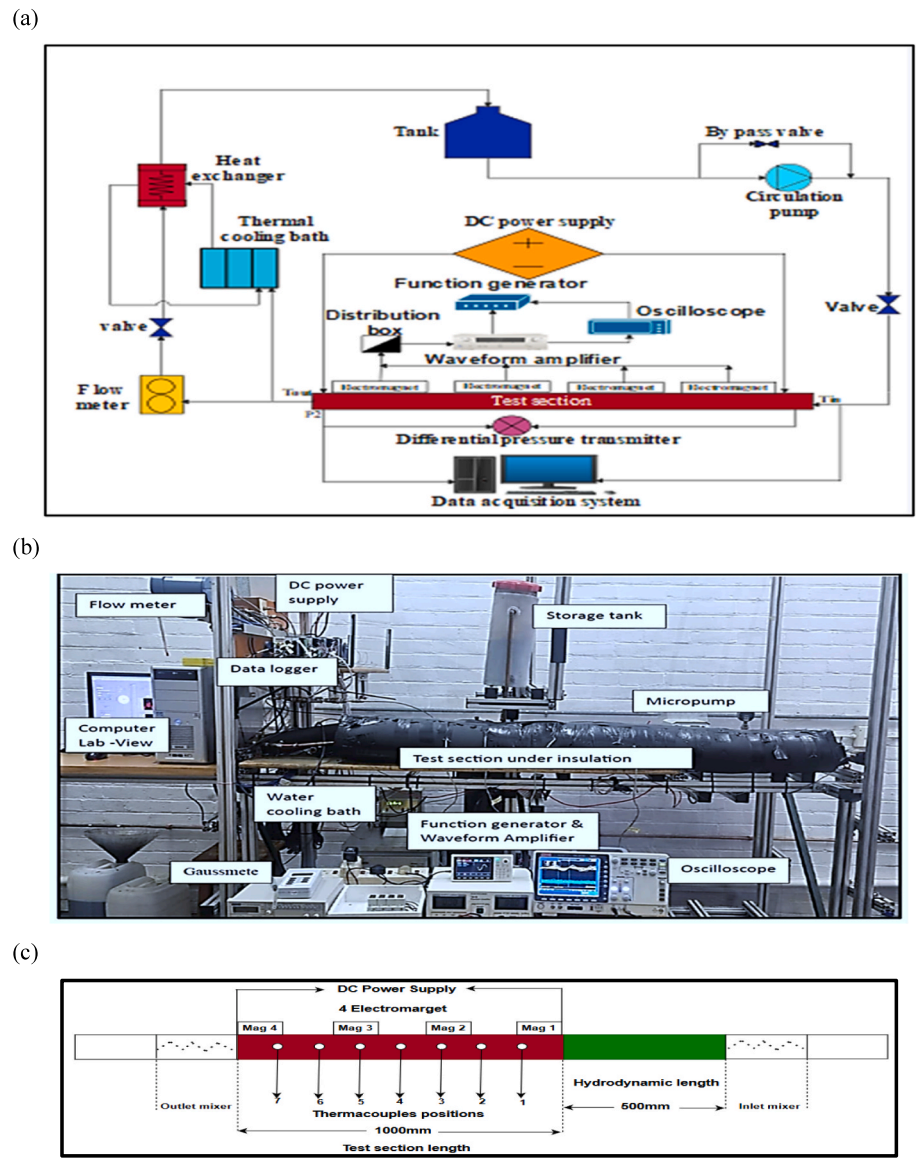


Figure: 7. (a) A diagram illustrating the experimental setup, (b) A breakdown of the test system's components, and (c) The arrangement of the experimental equipment, including electromagnets positioned along the copper tube.

the magnetic parameters were fine-tuned, and the system was stabilized (refer to Fig. 7)

3.3. Data reduction and uncertainty

The bulk fluid temperature was used to calculate density and specific heat capacity, following the methodology presented by Naike et al. [54], as demonstrated in Equations (9) and (10).

$$\rho_{nf} = (1-\varphi)\rho_{bf} + \varphi\rho_{np} \tag{9}$$

$$C_{pnf} = \frac{(1+\varphi)\rho_{bf}C_{pbf} + \varphi\rho_{np}C_{pnp}}{(1-\varphi)\rho_{bf} + \varphi\rho_{np}} \tag{10}$$

The energy input to the system is represented by Equation (11), and the corresponding thermal flux, determined from the power input to the system, is expressed in Equation (12) [55].

$$P = VI \tag{11}$$

$$Q = \dot{m}c_p(T_O - T_i) \tag{12}$$

The axial distribution of the local CHT efficiency for the fluids within the test rig was evaluated based on Newton's law of cooling, as expressed in Equation (13) [56].

$$h = \frac{Q}{A(t_w - t_b)} \tag{13}$$

The CHT coefficient of a fluid can be represented in terms of the *Nu*, which is evaluated using the following Equation (14).

$$Nu = \frac{hDi}{k} \tag{14}$$

The overall CHT coefficient ($h_{average}$) was determined by averaging the values calculated from the equations at the seven temperature sensor locations along the tube's length, as defined in Equation (15) (n = 7).

$$h_{aveg} = \frac{h_{(x1)} + \ldots\ldots\ldots\ldots\ldots\ldots h_{(xn)}}{n} \tag{15}$$

Equations (16) and (17) were applied to determine the Prandtl number (Pr) and Reynolds number (Re) for the trihybrid nanofluids.

$$\mathrm{Pr} = \frac{\mu c_p}{k} \tag{16}$$

$$\mathrm{Re} = \frac{4\dot{m}}{\pi D i} \tag{17}$$

Apart from examining heat transfer, this study assessed fluid resistance and the impact of the magnetic field on flow transformation within the test rig for both DIW and nanofluids. Additionally, the Colburn j-factor (j), thermal performance, and entropy generation were analysed. The study findings were juxtaposed with predicted flow resistance and the j-factor, determined using Equations (18) and (19).

$$f = \frac{\Delta P}{\left(\frac{L}{D}\right)\left(\frac{\rho v^2}{2}\right)} \tag{18}$$

$$\mathrm{j} = \frac{\mathrm{Nu}}{\mathrm{RePr}^{\frac{1}{3}}} \tag{19}$$

The thermal performance of the five nanofluid samples was evaluated across various Re to determine their suitability for practical thermal management applications. The study also examined the effect of the MF on the thermal exchange enhancement, as magnetic fields are known to influence the alignment and behavior of magnetic nanoparticles, thereby affecting the overall TC and CHT. The thermal Efficiency index (TEI) serves as a vital metric for evaluating the effectiveness of nanofluids in heat exchange systems. The mathematical representation of TEI is provided in Equation (20), as cited in Ref. [12].

Additionally, the total entropy generation rate (E_{gen}) within a cylindrical tube of length L is derived from the combined effects of frictional entropy generation ($E_{gen.fl}$) and thermal dissipation entropy ($E_{gen.Th}$). The overall entropy generation is determined by summing these individual components, as detailed in Equations (21)–(24) [57].

$$\eta = \frac{\frac{h_{avg.bf}}{h_{avg.nf}}}{\frac{\Delta P_{nf}}{\Delta P_{bf}}} \tag{20}$$

$$\dot{E}_{gen} = E_{gen.Th} + E_{gen.fl} \tag{21}$$

$$E_{gen.Th} = \frac{\pi d^2 L q^{-2}}{K_{nf} Nu T_{av}} \tag{22}$$

$$E_{gen.fl} = \frac{32\dot{m}^2 fl}{\rho_{nf}^2 \pi^2 d^5 T_{av}} \tag{23}$$

$$T_{avg} = \frac{(T_{in} - T_{out})}{In\left(\frac{T_{in}}{T_{out}}\right)} \tag{24}$$

3.4. Nusselt number validation

In this investigation, deionized water (DIW) was utilized to validate the experimental setup, with measurements taken across both laminar and turbulent flow. The data collected in the turbulent flow region in contrast to established correlations from and Sieder and Tate [58], Dittus Boelter [59], and Gnielinski [60], as shown in Fig. 8 and expressed in Equations (25) and (26). The findings revealed that the Gnielinski model slightly underestimated the experimental findings, with a deviation of less than 3 % in the turbulent flow regime. Both the Dittus–Boelter and Sieder and Tate models aligned closely with the study data. However, the Gnielinski equation provided the most accurate results, consistently underpredicting by an average of under 3 %. This validation underscores the precision of the experimental setup and reinforces the dependability of the findings in the turbulent flow regime (see Fig. 9).

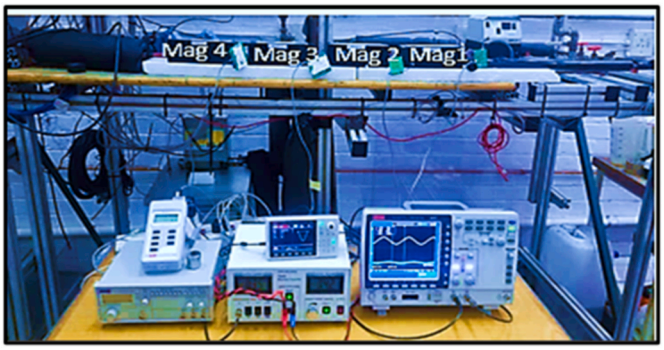


Fig. 8. Schematic representation of magnetic field arrangement.

$$3 \le \frac{x}{D} \le 192; 7000 \le 49000; 4 \le Pr \le 34; 1.1 \le \frac{u}{u_w} \le 1.7$$

$$\text{Nusselt number} = 0.026.Re^{0.788}.Pr^{\frac{1}{3}}.\left(\frac{u_b}{u_w}\right)^{0.4} \tag{26}$$

3000 e ≤17800 and 3.73 ≤ Pr ≤ 5.06

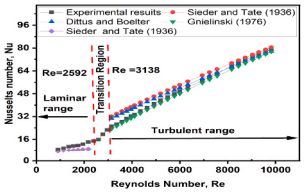


Fig. 9. Experimental Data versus predicted results from theoretical models.

$$\text{Nusselt number} = 0.026.Re^{0.8}.Pr^{0.385}.\left(\frac{x}{D}\right)^{-0.0054}\left(\frac{u}{u_w}\right)^{0.4} \tag{25}$$

$$3 \le \frac{x}{D} \le 192; 7000 \le 49000; 4 \le Pr \le 34; 1.1 \le \frac{u}{u_w} \le 1.7$$

$$\text{Nusselt number} = 0.026.Re^{0.788}.Pr^{\frac{1}{3}}.\left(\frac{u_b}{u_w}\right)^{0.4} \tag{26}$$

3000 e ≤ 17800 and 3.73 ≤ Pr ≤ 5.06

3.5. Uncertainty analysis

The uncertainty in the experimental results was quantified at a 95 % confidence level, following the methods outlined by Dunn [61]. Uncertainties were evaluated under both high and low Reynolds number conditions, with Re values of 5000 and 1000, respectively, using procedures similar to those described by Osman et al. [62] and Meyer [63]. At Re = 5000, the relative deviations observed in the *Nu*, Re, heat transfer coefficient (h), were 4.6 %, 9 %, and 6.8 %, respectively. In contrast, for Re = 1000, the corresponding uncertainties were 3.6 % for h, 7.5 % for Re and for *Nu*, 5.3 %.

$$\frac{\delta Nu}{Nu} = \sqrt{\left(\frac{\partial h_{avg}}{h_{avg}}\right)^2 + \left(\frac{\partial D_h}{D_h}\right)^2 + \left(\frac{\partial k}{k}\right)^2} \tag{27}$$

$$\frac{\delta Re}{Re} = \sqrt{\left(\frac{\partial \rho}{\rho}\right)^2 + \left(\frac{\partial V}{V}\right)^2 + \left(\frac{\partial D_h}{D_h}\right)^2 + \left(\frac{\partial \mu}{\mu}\right)^2} \tag{28}$$

$$\partial h(x) = \sqrt{\left(\frac{\partial h(x)}{\partial \dot{q}}\delta\dot{q}\right)^2 + \left(\frac{\partial h(x)}{\partial T_s}\delta T_s\right)^2 + \left(\frac{\partial h(x)}{\partial T_m}\delta T_m\right)^2} \tag{29}$$

4. Results and discussion

This section presents the empirical data collected during the

experiments, followed by a comprehensive discussion of the results. The study investigates the effect of various factors such as temperature variation, nanoparticle volumetric fraction, and flow conditions on the CHT performance of the nanofluid. Additionally, the role of magnetic field application and Re on the thermal exchange and flow properties is explored, particularly focusing on the transition phase were flow shifts from laminar to turbulent. This transition is critical in understanding the thermal exchange dynamics of the nanofluid under real-world conditions, as it influences both energy efficiency and fluid behavior.

4.1. Effect of nanoparticle volumetric ratio and MF waveforms on convective heat transfer performance in the transition and turbulent regimes

This study systematically evaluated the CHT performance of THNFs nanofluids at different nanoparticle volume fractions, as depicted in Fig. 10a and b, which present the *Nu* against Re and the average thermal transport coefficient against Re. The investigated volume fractions were 0.0025 vol%, 0.1 vol%, 0.2 vol%, 0.3 vol%, and 0.4 vol%, using DIW as the baseline fluid in the absence of a magnetic field. The percentage improvements in heat transfer relative to DIW, as shown in **Figure i**, were determined to be 2.89 %, 4.19 %, 10.49 %, 14.63 %, and 0.73 % for 0.0025 vol%, 0.1 vol%, 0.2 vol%, 0.3 vol%, and 0.4 vol%, respectively, in the turbulent flow regime. These results indicate that while a very small nanoparticle addition (0.0025 vol%) provides only a marginal improvement, increasing the concentration beyond 0.3 vol% (as seen in 0.4 vol%) leads to performance degradation due to the rise in viscosity, which counteracts the TC enhancement.

In the transition regime (Re between 2300 and 4000), the highest augmentation in CHT was observed at a nanoparticle concentration of 0.05 vol%, yielding a 29.49 % enhancement. This was followed closely by 0.3 vol% and 0.2 vol%, which showed enhancements of 28.48 % and 28.56 %, respectively. Lower volume fractions, including 0.1 vol% and 0.025 vol%, demonstrated improvements of 24.85 % and 10.38 %, respectively. These results suggest that 0.3 vol% offers optimal equilibrium between thermal conductivity improvement and increased viscosity-induced resistance.

With the introduction of a MF, the effect of various waveform types

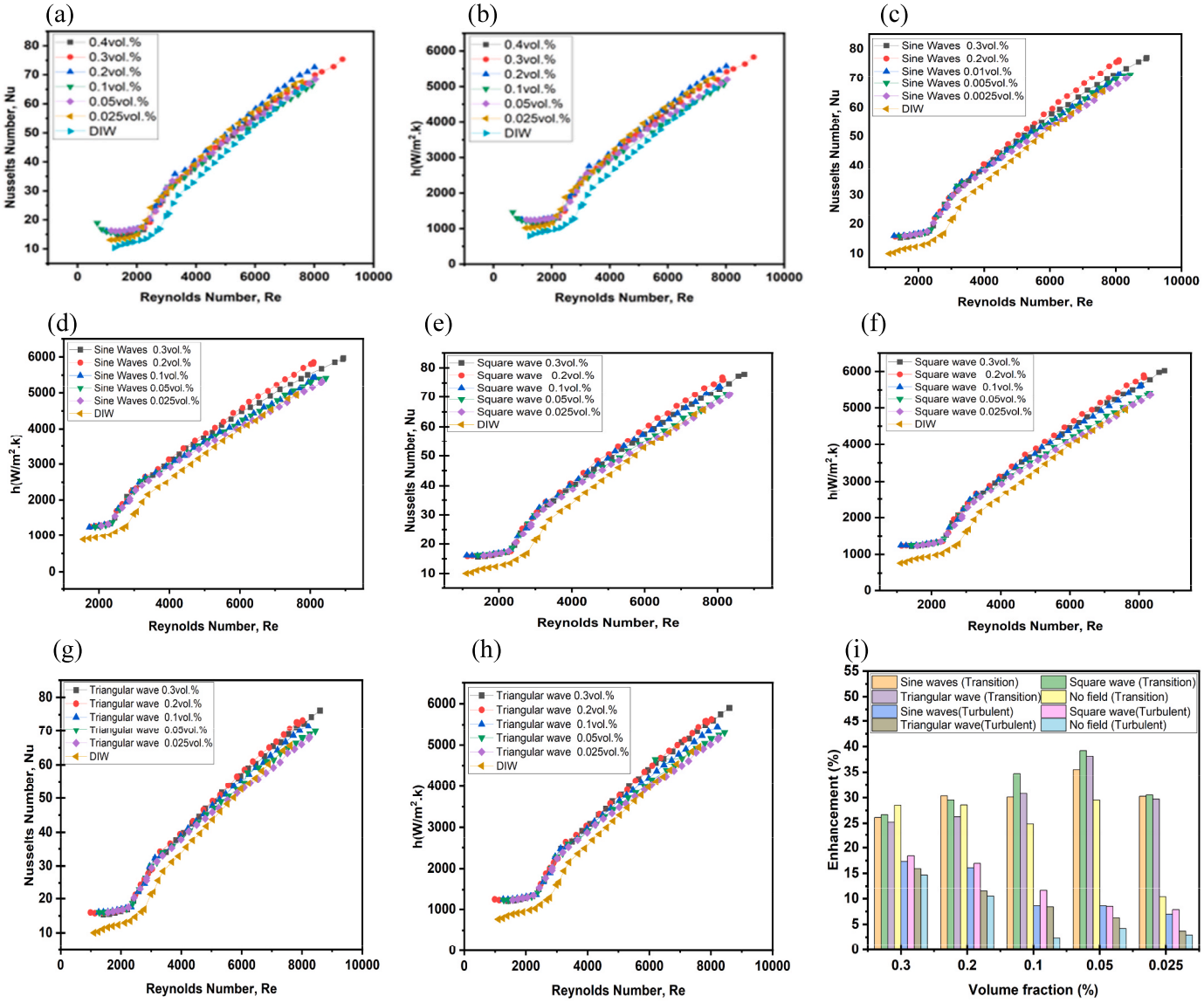


Fig. 10. Enhancement of CHT in THNFs (a) & (b) Nusselt number and average thermal exchange coefficient vs. Re for various nanoparticle volume fractions (Without magnetic field) (c) & (d) Heat transfer enhancement under Sine wave magnetic field in the entire regime (e) & (f) Heat transfer improvement under Square wave magnetic field in the entire regime (g)& (h) Heat transfer enhancement under Triangular wave magnetic field in the entire (i) Percentage enhancement comparism with transition and turbulent.

on thermal exchange performance was analysed. In the transition regime, under sine wave excitation, as depicted in Fig. 10c and d, heat transfer improvements were recorded as 26.11 %, 30.34 %, 30.11 %, 35.5 %, and 30.26 % for 0.3 vol%, 0.2 vol%, 0.1 vol%, 0.05 vol%, and 0.025 vol%, respectively. When subjected to square wave excitation, as illustrated in Fig. 10e and f, the enhancements were slightly higher, with values of 26.68 %, 29.50 %, 34.72 %, 39.21 %, and 30.48 % for the same volume fractions. Similarly, triangular waves, as shown in Fig. 10g and h, yielded enhancements of 25.22 %, 26.26 %, 30.79 %, 38.13 %, and 29.67 %, respectively. The data indicate that although square waves generally led to in the highest augmentation, the differences in thermal transport enhancement among waveform types were not significantly large in the transition regime.

In the turbulent regime, as presented in Fig. 10i, the effect of magnetic waves led to lower overall enhancements compared to the transition regime. Under sine wave excitation, the heat transfer enhancements were 17.34 %, 16.08 %, 8.58 %, 8.58 %, and 6.97 % for 0.3 vol%, 0.2 vol %, 0.1 vol%, 0.05 vol%, and 0.025 vol%, respectively. Square wave excitation produced slightly greater improvements, with corresponding values of 18.42 %, 16.92 %, 11.62 %, 8.49 %, and 7.89 %. The triangular wave configuration exhibited the lowest enhancements, with values of 15.91 %, 11.48 %, 8.40 %, 6.27 %, and 3.68 % for the respective volume fractions. These findings indicate that while the enhancements were smaller in the turbulent regime, square wave excitation provided a slight advantage over the other waveform types.

From a magnetohydrodynamic (MHD) perspective, the square waveform's pulsed structure rapidly switches the magnetic field on and off, generating alternating Lorentz forces that disrupt the boundary layer and enhance mixing. These sharp pulses induce localized eddy currents, promoting microscale turbulence and nanoparticle redistribution within the flow. The repeated acceleration and deceleration of charged nanoparticles improve convective energy transport while reducing localized stagnation zones. This mechanism underlies the superior heat transfer performance observed under square wave excitation, compared to the smoother sinusoidal or triangular alternatives.

Overall, this study concludes that a nanoparticle concentration of 0.3 vol% is optimal for enhancing convective heat transfer in trihybrid nanofluids across both the transition and turbulent flow regimes. At this concentration, the benefits of increased thermal conductivity outweigh the adverse effects of viscosity.

Furthermore, our findings indicate that a nanoparticle concentration of 0.3 vol% offers optimal performance across both transition and turbulent flow regimes. At this level, the increase in thermal conductivity sufficiently outweighs any viscosity-related drawbacks.

The observed trends are supported by the following mechanisms.

- Enhanced Thermal Conductivity: The ternary combination leverages the high intrinsic thermal conductivities of MWCNT, Fe_3O_4 and Al_2O_3, forming interconnected thermal pathways that promote rapid heat diffusion. This effect is most prominent at 0.3 vol%, where the synergy between nanoparticles results in superior heat transfer while maintaining manageable flow resistance.
- Brownian Motion: As nanoparticle concentration and fluid velocity increase, intensified Brownian motion of the nanoparticles promotes localized mixing at the microscale, leading to enhanced thermal dispersion and energy transport.
- Nanolayer Effects: At the solid–liquid interfaces of nanoparticles, structured interfacial liquid layers form, exhibiting higher thermal conductivity than the base fluid. These nanolayers contribute significantly to the overall thermal transport, particularly under turbulent flow conditions.
- Momentum and Thermal Diffusivity Improvements: The increasing Reynolds number implies stronger inertial forces, which improve fluid mixing and reduce thermal boundary layer thickness. This facilitates better convective heat exchange throughout the fluid domain.

Collectively, these phenomena account for the enhanced Nusselt number behavior observed in our study, particularly under square wave magnetic excitation, which intensifies nanoparticle agitation and thermal boundary disruption.

Furthermore, applying a magnetic field, particularly with square wave excitation, significantly influences heat transfer performance, suggesting its potential for optimizing thermal system efficiency in practical applications. In summary, this study identifies 0.3 vol% THNF under square wave magnetic field excitation as the optimal configuration, achieving high heat transfer performance without excessively penalizing system pressure. Incorporating MHD-based physical interpretations, such as Lorentz force dynamics and nanoparticle reorganization, provides valuable mechanistic insight. These findings support the targeted design of nanofluid-based thermal systems, especially in energy-efficient industrial and electronics cooling applications.

4.2. Flow regime transitions

4.2.1. Onset of the transitional flow with THNFs without magnetic field and magnetic field

The onset of the transitional flow regime, marking the end of the laminar regime, is identified as Re_{cr}, following a methodology similar to Evert and Meyer [64] and Ghajar and Tam [65] as outlined in Equation (18).

$$\mathrm{Re} = \mathrm{Re}_{cr}, \text{ when } \mathrm{Re} = \left(\frac{dj}{dRe}\right) = 0 \tag{18}$$

The value of Re is considered equal to Re_{cr} when the rate of change of the Colburn j-factor with respect to Reynolds number, $\frac{dj}{dRe}$, is calculated at any arbitrary point, i, using the data from three Reynolds numbers. Based on our experimentation, three data points typically provided the most reliable results. In Fig. 11, the gradient of the Colburn j-factor, $\frac{dj}{dRe}$, is shown as a relation of Re and a heat flow of 8.67 kW/m^2 in the 1500 mm test rig. From this plot, the critical Reynolds number, at which the flow transitions from laminar to turbulent, is found to be 2304 for DIW as shown in Fig. 11 a. This transition is marked by a change in the gradient of $\frac{dj}{dRe}$ from negative to positive.

The critical Re, which marks the transition from laminar to turbulent flow, varies depending on the presence of a magnetic field and the waveform applied. As deplicted in Fig. 11a, for DIW, the critical Re is found to be 2304. However, when using THNFs without a MF, the transition Re shifts as follows.

- 0.3 vol% – Re = 2257.03 (Fig. 11b)
- 0.2 vol% – Re = 2450.63 (Fig. 11c)
- 0.1 vol% – Re = 2121.95 (Fig. 11d)
- 0.05 vol% – Re = 2225.25 (Fig. 11e)
- 0.025 vol% – Re = 2026.99 (Fig. 11f)

These variations arise due to the interplay between enhanced viscosity and thermal conductivity at different nanoparticle volume fractions. Higher concentrations (e.g., 0.2 vol%) tend to delay transition due to increased viscosity, while lower concentrations (0.025 vol%) promote earlier transition due to weaker momentum diffusion and flow destabilization.

Effect of Magnetic Field on Transition Reynolds Number.

When a sine wave magnetic field is introduced, the transition onset shifts (as shown in Fig. 11i to j).

- 0.3 vol% – Re = 2220.36
- 0.2 vol% – Re = 2319.44
- 0.1 vol% – Re = 2301.13
- 0.05 vol% – Re = 2368.10
- 0.025 vol% – Re = 2264.48

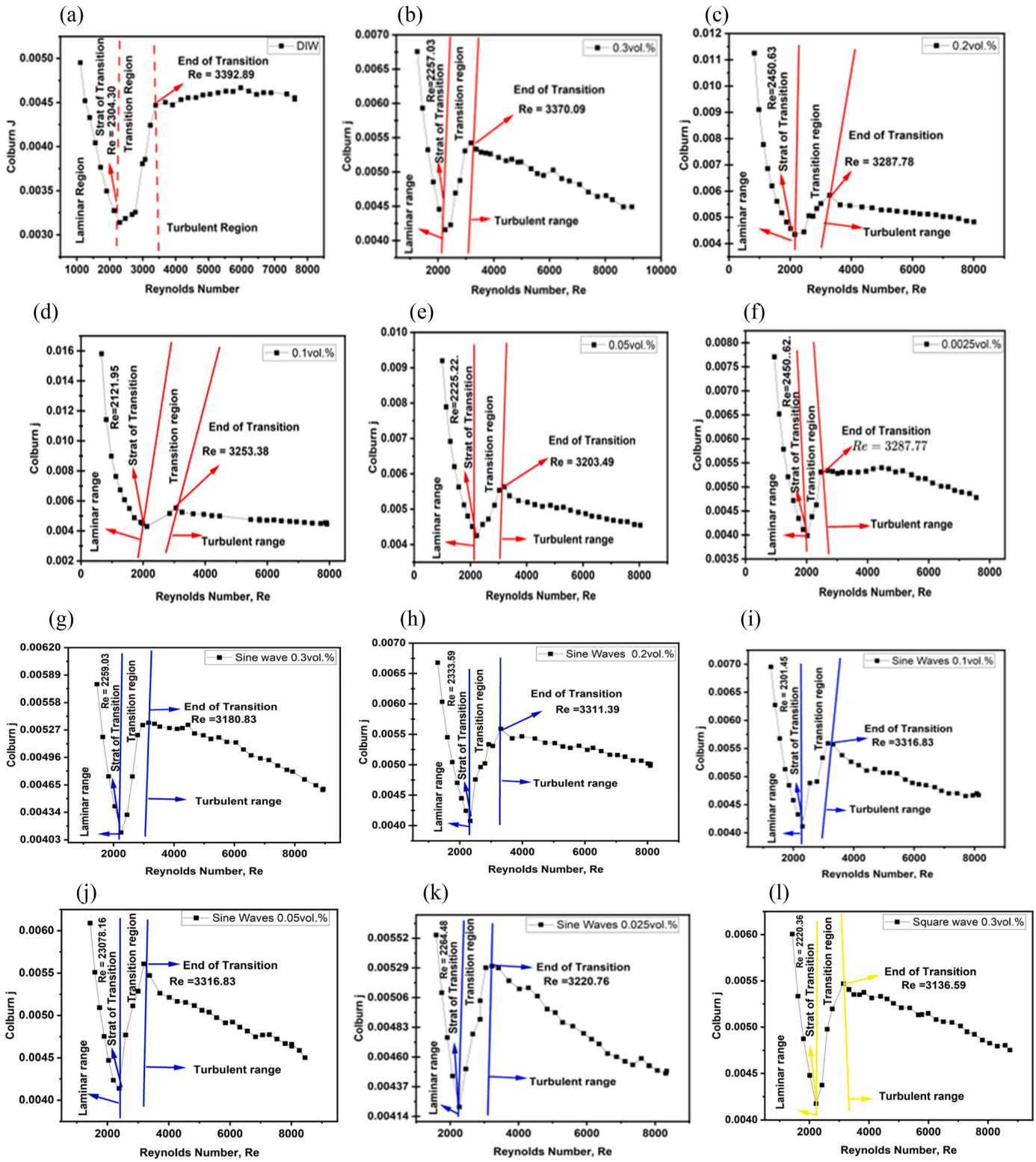


Fig. 11. Effect of nanoparticle volumetric ratio and magnetic field waveforms on the onset of transition from laminar to turbulent flow in ternary nanofluids

The sinusoidal oscillations of the magnetic field create periodic Lorentz forces, which enhance stability by evenly redistributing momentum and delaying transition. However, at lower concentrations, the effect is less pronounced due to weaker nanoparticle interactions with the magnetic field.

For square wave excitation (Fig. 11L to p), the transition Reynolds numbers are.

- 0.3 vol% – Re = 2259.03
- 0.2 vol% – Re = 2333.59
- 0.1 vol% – Re = 2301.45
- 0.05 vol% – Re = 23078.16

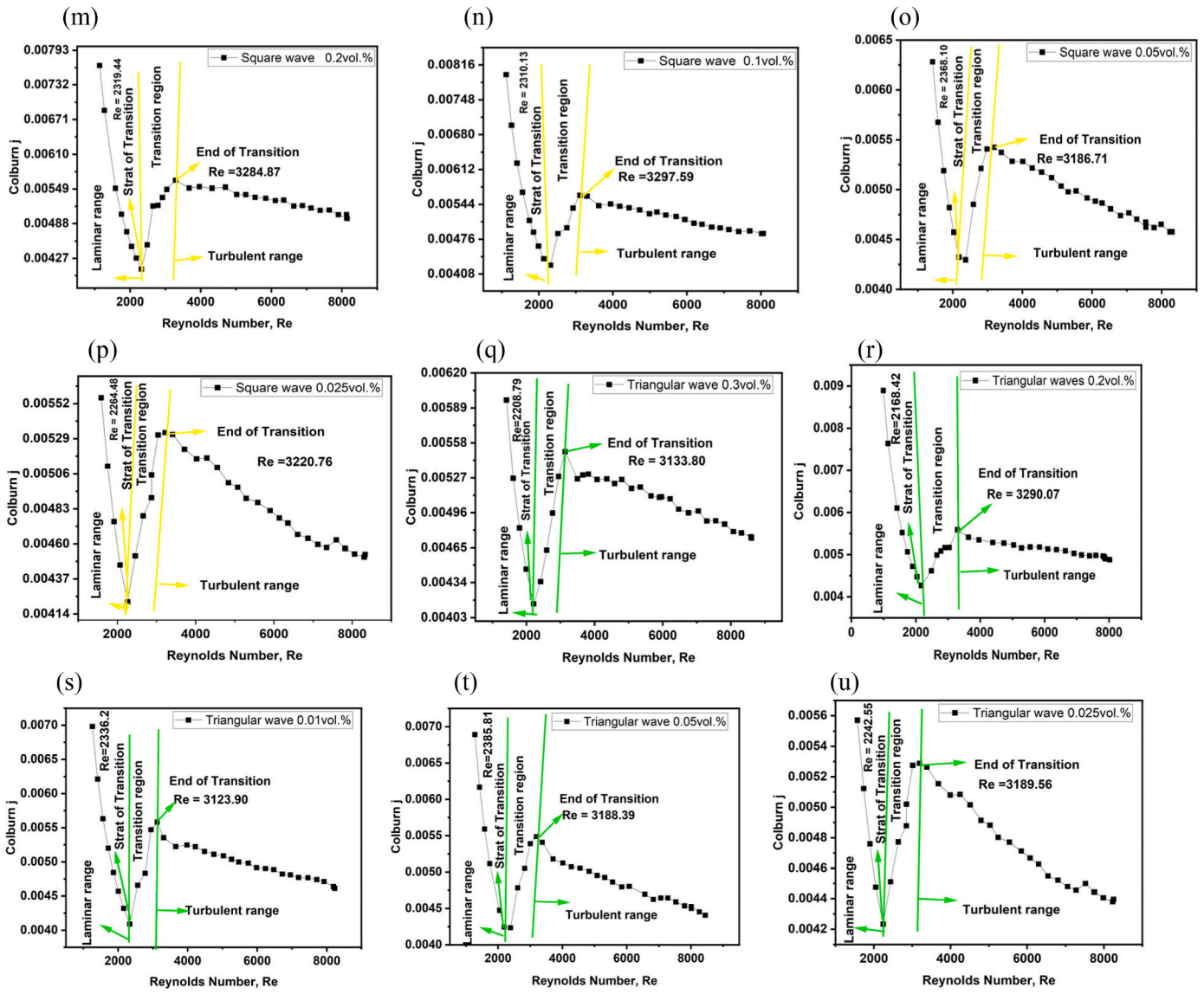


Fig. 11. (*continued*).

- 0.025 vol% – Re = 2264.48

Square waves generate abrupt magnetic field fluctuations, causing rapid velocity perturbations that induce early transition. This leads to more aggressive flow mixing compared to sine waves, especially at lower volume fractions.

For triangular wave excitation (Fig. 11q to u), the transition Reynolds numbers are.

- 0.3 vol% – Re = 2208.79
- 0.2 vol% – Re = 2168.42
- 0.1 vol% – Re = 2336.20
- 0.05 vol% – Re = 2385.81
- 0.025 vol% – Re = 2245.55

Triangular waves create a gradual increase and decrease in magnetic field strength, providing a balance between flow stabilization and induced turbulence. The highest transition Reynolds number (2385.81 at 0.05 vol%) indicates that triangular waves can effectively delay turbulence onset under specific volume fractions, offering moderate stabilization compared to sine waves but less aggressive perturbations than square waves.

Without a magnetic field, the transition Reynolds number (Re) is primarily influenced by nanoparticle volume fraction. Higher concentrations, such as 0.2 vol%, tend to delay the transition due to increased viscosity effects, whereas lower concentrations, such as 0.025 vol%, promote early turbulence by reducing flow resistance. When a sine wave magnetic field is applied, it creates smooth periodic momentum redistribution, generally stabilizing flow structures and delaying the transition onset. In contrast, a square wave magnetic field produces sharp velocity perturbations, which induce stronger turbulence and lead to an earlier transition. The triangular wave magnetic field provides a more balanced stabilization effect, with transition delays varying based on specific volume fractions. Overall, the application of a magnetic field serves as an active control mechanism for the transition regime, where square waves enhance turbulence induction, while sine and triangular waves contribute to flow stabilization to different degrees. These findings are crucial for optimizing thermal-fluid systems that incorporate hybrid nanofluids under magnetic excitation.

4.3. Impact of nanoparticle concentration, magnetic field on the pressure drop characteristics of nanofluids in the transition flow regime

The pressure drop characteristics of the nanofluids, in the absence of

an MF, reveal important insights into the influence of nanoparticle volume fraction and Re on flow resistance. As seen in Fig. 12a, at higher Reynolds numbers (e.g., Re ≈ 8951 for 0.3 vol%), the pressure drop reaches approximately 0.000635, which is the highest among the tested concentrations. In contrast, at a similar Reynolds number for DIW, the pressure drop is lower at 0.000545, confirming that nanoparticle addition increases flow resistance. This increase is attributed to the higher viscosity of nanofluids, leading to greater frictional losses compared to DIW.

For moderate Re (e.g., Re ≈ 3180 for 0.3 vol%), the pressure drop is around 0.000215, significantly higher than that of lower nanoparticle concentrations. For instance, the 0.2 vol% nanofluid at the same Reynolds number exhibits a reduced pressure drop of 0.000154, while DIW shows an even lower value of 0.000180. This further highlights the viscosity-induced penalty from higher nanoparticle loading. At the lowest Reynolds number in the dataset (≈1253 for 0.3 vol%), the pressure drop falls to 7.79E-05, further demonstrating the trend of reduced pressure loss at low flow rates.

At lower volume fractions (e.g., 0.0025 vol%), the pressure drop remains closer to that of DIW across all Reynolds numbers, with only slight deviations, especially in the transition region. For example, at Re ≈ 2449, the pressure drop for 0.0025 vol% is 0.000121, while for DIW, it is 0.000133, showing minimal variation. However, for 0.3 vol%, the pressure loss at the same Re is significantly higher at 0.000161, confirming that higher nanoparticle concentrations lead to an increase in shear resistance this in aligned with Kanti et al. [66]. The transition flow regime plays a critical role in pressure drop behavior, where a sharp increase is observed, particularly for nanofluids with higher concentrations, suggesting that turbulence onset occurs earlier compared to DIW. This earlier transition is attributed to nanoparticle interactions, which enhance flow disturbances and modify the critical Reynolds number for transition. This phenomenon illustrates the trade-off: while nanofluids enhance heat transfer performance, they also introduce increased pressure drop, which must be carefully considered for practical applications in thermal systems.

The introduction of a MF alters these characteristics further, intensifying the pressure drop behavior due to the magnetizable nature of the nanoparticles. Magnetic fields influence the alignment and aggregation of nanoparticles, significantly affecting viscosity, flow behavior, and the onset of turbulence. As the magnetic field strength increases, it leads to more pronounced nanoparticle clustering, which further increases the fluid's effective viscosity and, consequently, the pressure drop. This effect is most prominent at higher nanoparticle concentrations, where the added viscosity from both the nanoparticles and the MF leads to greater frictional losses.

In the presence of oscillatory motion, such as sine, square, and triangular waves, the flow resistance and pressure drop are impacted in distinct ways. Fig. 12b reveals that higher nanoparticle concentrations, like 0.3 vol%, result in a higher pressure loss across all Re compared to lower concentrations and DIW. For example, at Re ≈ 8940, the pressure drop for the 0.3 vol% nanofluid is 0.000633, compared to 0.000545 for DIW. The introduction of sine waves significantly alters the flow characteristics, influencing the pressure drop at different Re. As the Re increases, the pressure drop follows a trend typical of transition flow behavior. Higher nanoparticle concentrations (0.3 vol%) show a sharper increase in pressure drop, suggesting that sine waves enhance flow instability and induce earlier transitions to turbulence. The oscillations likely disturb the boundary layer, increasing shear forces and energy dissipation, which leads to higher pressure losses in nanofluid cases. At lower Reynolds numbers (e.g., Re ≈ 2446 for 0.3 vol%), the pressure drop is 0.000159, higher than DIW (0.000120) but lower than at higher Reynolds numbers. This suggests that in laminar flow conditions, sine wave oscillations may slightly dampen pressure losses, unlike in transition or turbulent regimes, where they amplify instabilities.

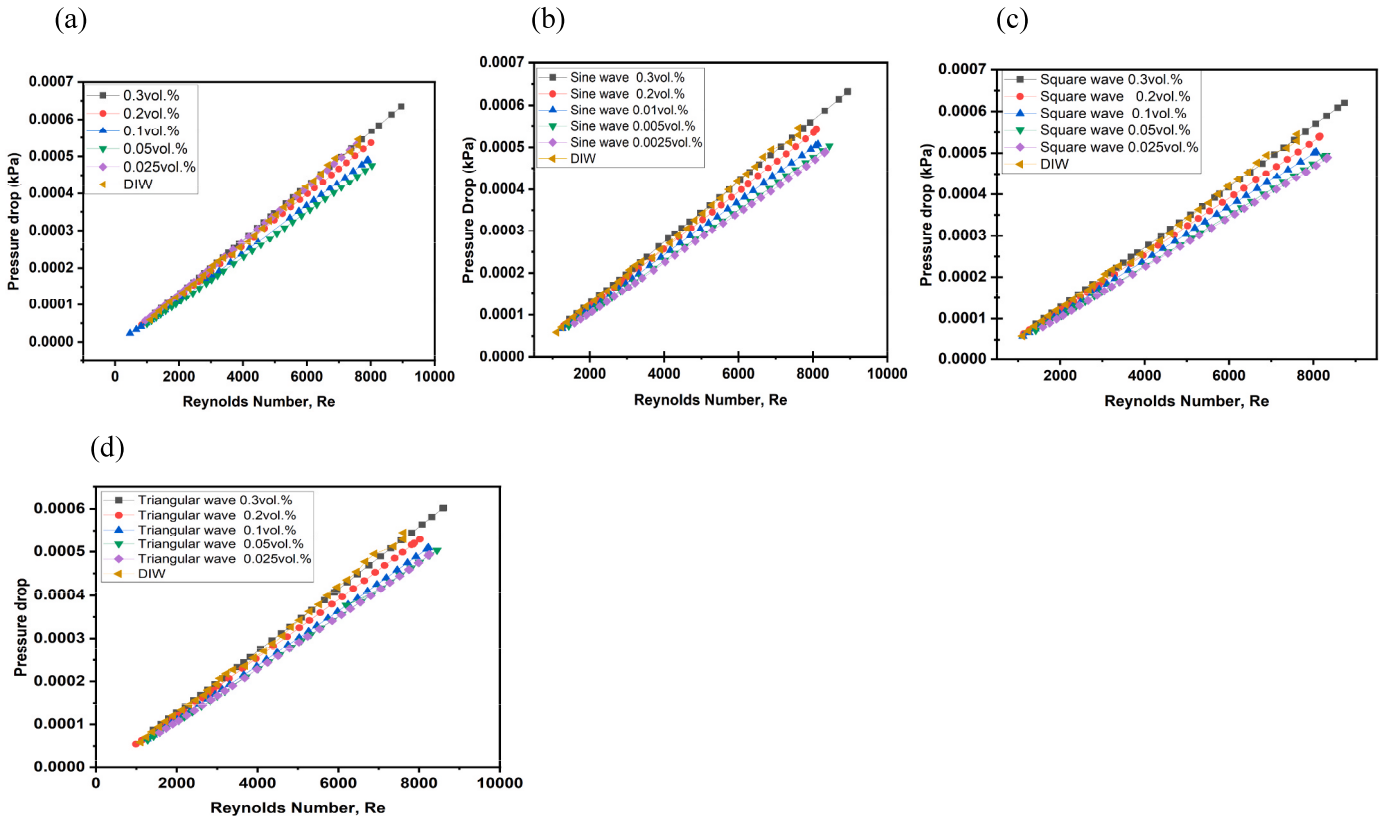


Fig. 12. Pressure decline properties of nanofluids across multiple nanoparticle concentrations and Re under the influence of MF (a) Pressures without MF (b) Pressure decline with Sine wave (c) Pressure decline with Square wave (d) Pressure decline with Triangular wave.

Fig. 12c shows that when square wave oscillations are introduced, a noticeable reduction in pressure drop occurs across various Reynolds numbers. For instance, at Re ≈ 8734.7, the pressure drop for the square wave with 0.3 vol% nanoparticle concentration is 0.000620777, lower than the DIW value of 0.000545293. This trend continues across all Reynolds numbers and nanoparticle concentrations, with square wave oscillations consistently lowering the pressure drop compared to DIW. Square waves effectively enhance fluid flow by reducing flow resistance, improving mixing, and lowering pressure drop across different Reynolds numbers and nanoparticle concentrations.

When triangular wave oscillations are applied (Fig. 12d), the pressure drop decreases across a range of Reynolds numbers for various nanoparticle concentrations. At higher Reynolds numbers, such as Re ≈ 8602.95, the pressure drop for triangular waves with 0.3 vol% is 0.000602437, which is slightly higher than the square wave but still lower than the DIW value of 0.000545293. As the Reynolds number decreases, the pressure drop for triangular waves reduces further, with values such as 0.000389131 at Re ≈ 5655.14 for 0.3 vol% concentration. At lower Reynolds numbers, triangular wave oscillations show a more pronounced effect, reducing pressure drop as nanoparticle concentration decreases. For instance, at Re ≈ 2942.84, the pressure drop for triangular waves with 0.3 vol% concentration is 0.000193813, while for 0.05 vol% it is 0.000157261, indicating that lower concentrations lead to a more significant reduction in pressure drop. Similarly, at very low Reynolds numbers (Re ≈ 1794.54), the pressure drop for triangular waves with 0.3 vol% concentration is 0.000113447, and for 0.025 vol% it is 0.000100046, showing a consistent decrease as the concentration decreases.

In conclusion, the addition of nanoparticles to fluids increases viscosity and, consequently, flow resistance, resulting in higher pressure drops, especially in the transition flow regime. The application of oscillatory motion whether sine, square, or triangular waves further modulates the pressure drop. Square and triangular waves reduce the pressure drop, particularly at lower Reynolds numbers, due to enhanced mixing and better nanoparticle distribution. The MF influence, moreover, exacerbates the pressure loss by increasing the fluid's viscosity and promoting nanoparticle aggregation. Therefore, careful consideration of both MF strength and nanoparticle content is essential in optimizing flow characteristics in thermal applications.

4.4. Friction factor variation with Re for nanofluids under various oscillatory conditions

The friction coefficient is a nondimensional variable used to quantify the resistance to flow due to frictional effects within the system. It is derived from the measured pressure drop and is influenced by both the Reynolds number and the fluid's physical properties such as viscosity, which in this case is affected by nanoparticle concentration. As observed in Fig. 13a, at higher Reynolds numbers (for instance, around Re ≈ 8952 for 0.3 vol%), the friction factor is relatively low (≈7.15×10^{-9}), indicating lower frictional resistance in faster, more turbulent flows. Conversely, as the Re decreases and the flow shifts toward the laminar regime, the friction factor increases markedly; for example, at Re ≈ 1254 for DIW, the friction factor reaches approximately 5.79×10^{-8}.

Comparing different nanoparticle loadings, the friction coefficient shows subtle variations across similar Reynolds numbers. At Re ≈ 8952, the friction coefficient for the 0.3 vol% is slightly lesser than that for DIW, suggesting that nanoparticle addition can modify turbulent structures and effective viscosity in a manner that marginally reduces friction under high-flow conditions. However, as the flow rate decreases, the impact of nanoparticles becomes more pronounced, with higher concentrations generally resulting in increased frictional losses due to enhanced viscosity and altered flow behavior. Overall, these trends underscore the interplay between flow regime, nanoparticle concentration, and energy losses, offering essential insights for optimizing fluid dynamics in thermal and fluid transport applications.

When sine wave oscillations are introduced (Fig. 13b), the friction coefficient exhibits distinctive trends compared to non-oscillatory (DIW) conditions. For instance, at higher Reynolds numbers, the 0.3 vol% nanofluid under sine wave oscillations shows a friction factor of about

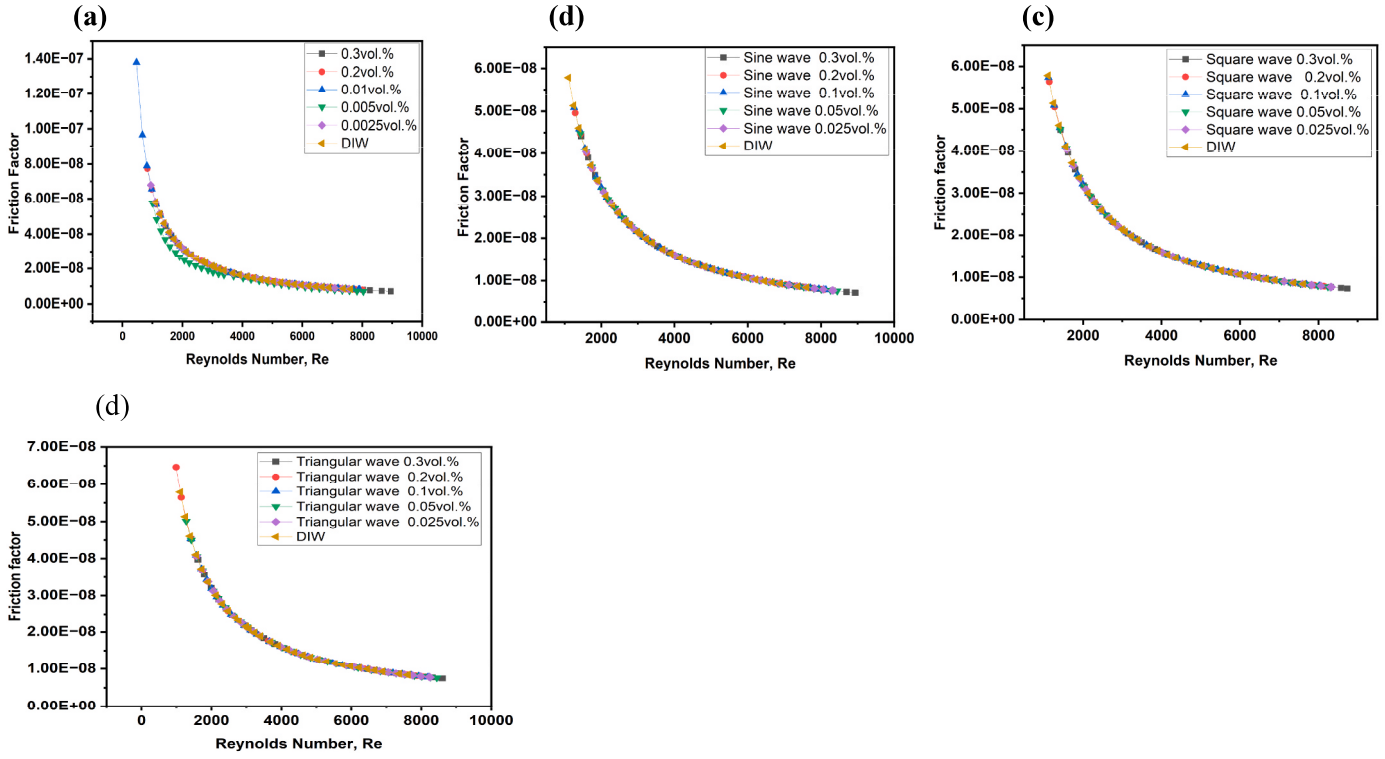


Fig. 13. Influence of nanoparticle concentration and oscillatory motion on the friction factor (a) friction factor with field (b) Sine wave (c) Square wave (d) Triangular.

7.16×10^{-9} at Re ≈ 8941, while DIW exhibits a higher friction factor of roughly 8.41×10^{-9} at a comparable Reynolds number (Re ≈ 7614). This reduction suggests that sine wave oscillations enhance mixing and disrupt boundary layer formation, thereby decreasing localized shear stresses and frictional losses. Across various nanoparticle concentrations with values for 0.2, 0.1, 0.05, and 0.025 vol% the friction factors remain in a similar range yet consistently tend to be lower than those for DIW under the same oscillatory conditions. As the Reynolds number decreases, all fluids experience an increase in the friction factor due to the growing influence of viscous forces; for example, the friction factor for a 0.3 vol% nanofluid increases to around 4.42×10^{-8} at Re ≈ 1450. Overall, sine wave oscillations not only modulate the friction factor by promoting beneficial flow dynamics but also reduce energy losses compared to pure water, especially in high-Reynolds-number regimes.

When square wave oscillations are introduced (Fig. 13c), the friction coefficient for nanofluids are consistently lower than those for DIW at comparable Re. For example, at a high Re 8734.70, the 0.3 vol% nanofluid under square wave oscillations exhibits a friction coefficient of about 7.33×10^{-9}, compared to 8.41×10^{-9} for DIW. This reduction indicates that square wave oscillations enhance mixing and disrupt the boundary layer, leading to a more uniform velocity profile and lower shear stresses at the wall. As the Re decreases, the friction coefficient increases for all cases due to the growing influence of viscous forces. At lower Reynolds numbers near 1421, the friction factor for the 0.3 vol% nanofluid rises to approximately 4.50×10^{-8}, while DIW shows a higher value of around 5.79×10^{-8}. Across different nanoparticle concentrations from 0.3 vol% down to 0.025 vol% the friction factors remain slightly lower than those of DIW, although the variations among the nanofluid cases are less pronounced. Overall, square wave oscillations effectively reduce frictional resistance in nanofluids by promoting flow dynamics that mitigate energy losses compared to a non-oscillatory baseline.

Finally, when triangular wave oscillations are introduced (Fig. 13d), the friction coefficient is notably influenced by both the Re and nanoparticle concentration. At higher Re, for example, the 0.3 vol% nanofluid under triangular wave oscillations shows a friction factor of approximately 7.44×10^{-9} at Re ≈ 8603, which is lower than the DIW value of about 8.41×10^{-9} at a similar Re. This reduction indicates that the periodic acceleration and deceleration from triangular oscillations enhance mixing and disrupt the boundary layer, thereby reducing localized shear stresses and frictional losses. As the Reynolds number decreases, the friction factor systematically increases due to the growing dominance of viscous forces for instance, at Re ≈ 1413, the friction factor for the 0.3 vol% nanofluid rises to roughly 4.53×10^{-8}, while DIW exhibits a higher friction factor of around 5.79×10^{-8}. Across different nanoparticle volume ratio (ranging from 0.3 vol% to 0.025 vol %), the friction coefficient under triangular wave conditions remain consistently lower than those for DIW, underscoring the role of oscillatory motion in promoting a more uniform velocity profile and enhancing momentum transport. Overall, triangular wave oscillations help reduce the effective friction factor by thinning the viscous sublayer and mitigating energy losses, particularly in high-Reynolds-number regimes, corroborating the findings of Chamkha et al. [67].

4.5. Total Efficiency Index: physical interpretation and practical implications

The Thermal Efficiency Index (TEI) offers a comprehensive evaluation of nanofluid performance by balancing the gains in heat transfer with the penalties of increased flow resistance. A TEI consistently greater than 1 across all waveforms and nanoparticle concentrations indicates that more thermal energy is transported per unit of pumping power compared to the base fluid (DIW). This highlights the potential of these nanofluids for practical implementation in systems such as microchannel heat sinks, compact heat exchangers, and electronic cooling applications.

For instance, in Fig. 14a, at 0.3 vol%, the TEI increases from 1.086 at higher flow rates (~0.0601) to 1.328 at lower flow rates (~0.0117). Although lower flow rates typically elevate entropy generation due to longer residence time, the enhanced thermal transport provided by nanoparticles reduces thermal gradients and irreversibility. Consequently, more of the input energy contributes to useful heat transfer, minimizing wasted energy and improving thermodynamic efficiency.

Under sine wave oscillations (Fig. 14b), the TEI at 0.3 vol% rises from 1.11 at ~0.06 to 1.39 at ~0.011, showing that boundary layer disruption and enhanced mixing significantly improve convective performance. This effect lowers both thermal and viscous entropy generation, thereby pushing the system toward more thermodynamically reversible operation. The improved mixing offsets the frictional losses, resulting in a net gain in system-level energy efficiency.

Similarly, square wave oscillations (Fig. 14c) produce a TEI of 1.13 at ~0.0587 for 0.3 vol%, representing a 13 % performance improvement over DIW. These oscillations create strong pulsations that break thermal stagnation zones and enhance momentum diffusion, reducing both temperature non-uniformity and viscous dissipation. Notably, even at lower nanoparticle loadings (0.05–0.025 vol%), the TEI remains above 1, confirming that performance gains are achievable without compromising stability or significantly increasing viscosity.

In the case of triangular wave excitation (Fig. 14d), the TEI at 0.3 vol % reaches 1.1128 at 0.05741, while values of 1.0959 and 1.0565 are observed at 0.2 and 0.1 vol%, respectively. This consistent behavior illustrates a positive thermodynamic trade-off: the enhancement in heat transfer through waveform-induced mixing more than compensates for the increased flow resistance, leading to lower entropy generation per unit of heat removed.

From a practical perspective, these results indicate that the combined use of ternary hybrid nanofluids and waveform-optimized magnetic fields enhances both thermal and thermodynamic efficiency. Across all tested conditions, useful energy output increases while entropy production is suppressed, translating into lower exergy destruction and improved sustainability. This makes such nanofluid systems suitable for deployment in advanced cooling technologies where energy efficiency, compact design, and high heat flux removal are critical.

In summary, the TEI, supported by entropy analysis, validates that these nanofluids not only boost convective heat transfer but do so in a thermodynamically favorable manner demonstrating both functional (enhanced cooling) and energetic (reduced irreversibility) advantages essential for next-generation thermal-fluid systems.

4.6. Thermal entropy generation in nanofluids under the impact of MF the effect of nanoparticle concentration and flow rate

Thermal entropy generation is a critical thermodynamic metric that quantifies irreversibilities in thermal systems—mainly arising from temperature gradients (heat transfer losses) and viscous dissipation (frictional effects). In thermal-fluid systems enhanced with nanoparticles and exposed to magnetic fields, this parameter becomes pivotal for understanding the trade-offs between heat transfer enhancement and the thermodynamic cost of such enhancements.

In the absence of a magnetic field (Fig. 15a), increasing nanoparticle concentration generally results in higher entropy generation. At first glance, this may appear counterintuitive, as nanoparticles enhance thermal conductivity and promote better heat transfer. However, physically, higher concentrations disturb the laminar flow profile more severely, leading to greater viscous dissipation due to elevated internal shear stresses. This explains why at a flow rate of 0.0601, entropy generation decreases slightly from 16.47 (at 0.0025 vol%) to 14.91 (at 0.3 vol%), but at lower flow rates like 0.035, the difference is more pronounced (27.49 vs. 22.17). The drop in flow rate increases fluid residence time, causing more extended contact with the heated wall, thereby enhancing entropy generation due to both prolonged heat exchange and frictional resistance this is consistence with exiting

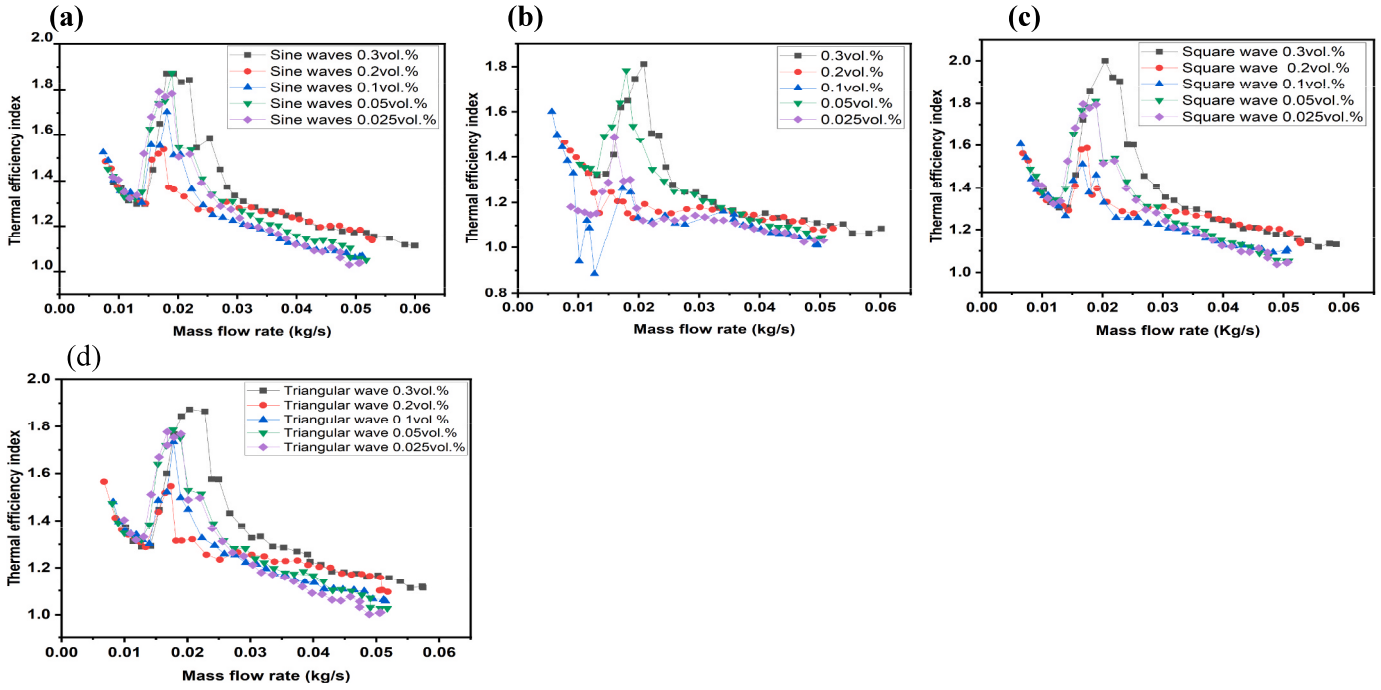


Fig. 14. a: Thermal efficiency index for various nanoparticle concentrations at different flow rates in baseline conditions (no oscillations) (b) Total efficiency index for various nanoparticle concentrations under sine wave oscillations at different flow rates (c) Total efficiency index for various nanoparticle concentrations under square wave oscillations at different flow rates (d) Total efficiency index for various nanoparticle concentrations under triangular wave oscillations at different flow rates.

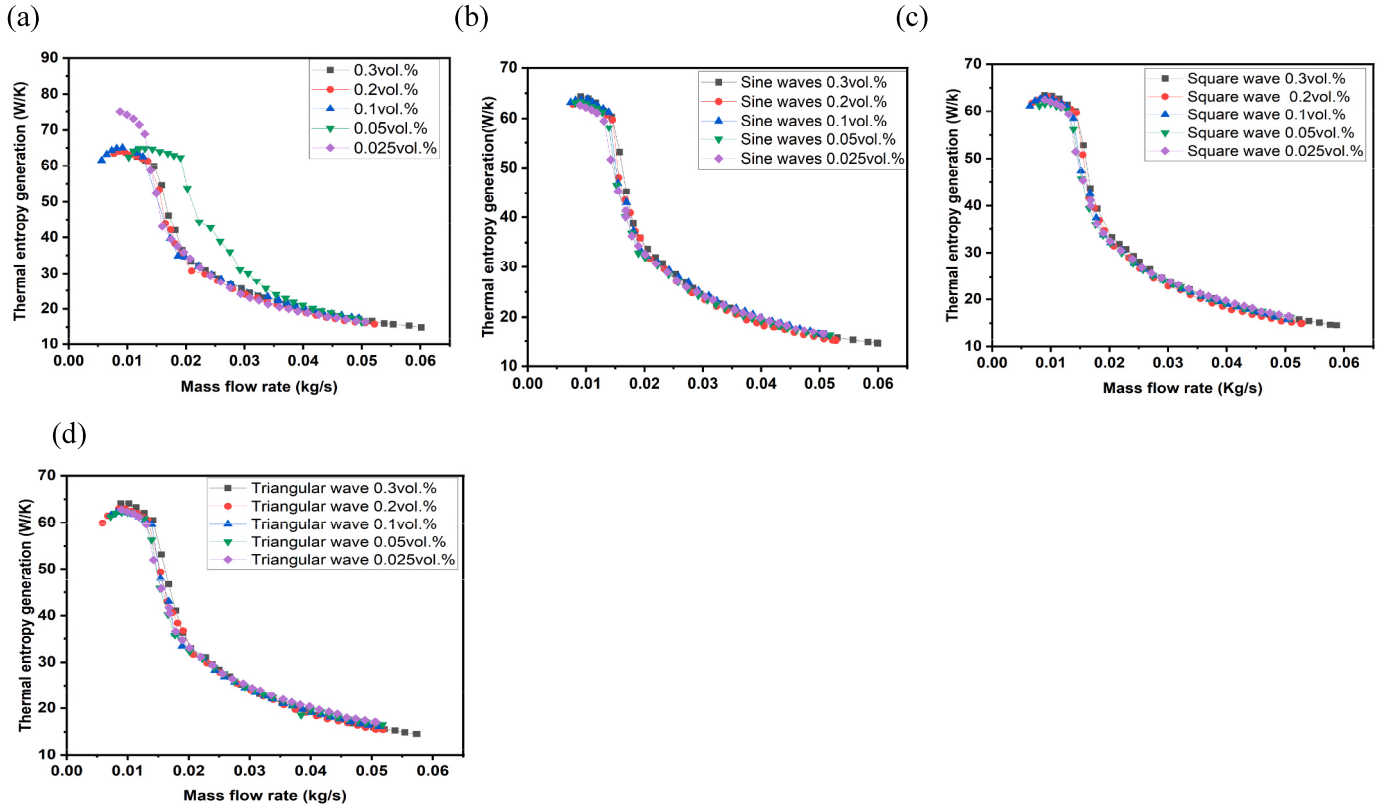


Fig. 15. Variation of thermal entropy generation in (a) With no fied (b) Sine,(c) Square and Triangular wave magnetic fields with nanoparticle concentration and flow rate.

litratureure [68].

When a sine waveform magnetic field is applied (Fig. 15b), the field introduces cyclical disturbances that enhance mixing and thermal boundary layer disruption. These actions improve convective heat transfer but also amplify frictional losses, especially at lower flow rates. For instance, at 0.3 vol% and 0.0601 flow rate, entropy generation is 14.54, but dramatically increases to 64.34 when the flow rate drops to 0.0091. This signifies that while thermal performance improves, it comes at the expense of thermodynamic efficiency.

Square waveform magnetic fields (Fig. 15c) intensify this effect by generating abrupt field transitions, inducing transient micro-vortices that further disrupt flow symmetry. This turbulence enhances heat transfer, yet the sharp changes result in significant entropy spikes due to unsteady shear flows. For 0.3 vol%, entropy generation jumps from 14.55 at 0.0587 to 63.45 at 0.0089. The increase demonstrates how field-induced turbulence although beneficial for heat transfer can degrade system efficiency through irreversibility.

Similarly, triangular waveform magnetic fields (Fig. 15d) exert a continuous yet milder modulation. At 0.3 vol% and flow rate 0.05741, entropy starts at 14.56 and rises to over 64 as flow reduces to 0.00887. The increase remains consistent across lower concentrations, such as 0.05 vol% and 0.025 vol%, affirming that flow rate is a dominant parameter affecting entropy production across all field types and concentrations.

Physically, this behavior underlines a fundamental thermodynamic trade-off: magnetic field waveforms and higher nanoparticle loading enhance convective performance by disrupting thermal resistances but simultaneously introduce frictional and shear-related losses that raise entropy. Therefore, the challenge is to optimize operating parameters to maximize heat transfer (Nusselt number) while minimizing entropy generation to ensure net thermal efficiency.

In summary, thermal entropy generation in magnetically influenced nanofluid systems reflects the irreversible penalty paid for performance gains. Its practical interpretation extends beyond numbers it signifies where and how energy is being degraded and guides the design of thermodynamically optimal systems.

4.7. Frictional entropy generation in nanofluids under different MF conditions and the impact of nanoparticle content and flow rate

Frictional entropy generation represents the irreversible loss of mechanical energy due to viscous dissipation as fluid flows through a conduit. In nanofluids, the addition of nanoparticles increases viscosity and introduces microscopic disturbances in the flow, leading to greater internal friction. These effects directly elevate entropy generation, reflecting energy losses that cannot be recovered for useful work thus reducing the thermal system's overall efficiency.

In the absence of a magnetic field (Fig. 16a), entropy generation increases as the flow rate decreases. This is because reduced flow velocity extends the residence time of the fluid within the channel, increasing the duration over which frictional forces act. At higher flow rates, fluid moves more swiftly with less time for viscous dissipation, hence the lower entropy values observed. The trend highlights a fundamental trade-off: slower flow may improve heat transfer via extended wall contact but does so at the cost of greater frictional irreversibility.

When a sine wave magnetic field is applied (Fig. 16b), the periodic Lorentz forces modulate the flow profile dynamically, causing time-varying shear stresses especially near the walls. These oscillations enhance mixing but also lead to additional entropy generation due to cyclic velocity gradients. For example, for a 0.3 vol% nanofluid, frictional entropy generation is $\sim 6.81 \times 10^{-9}$ at 0.05999 m/s, reducing to $\sim 3.92 \times 10^{-9}$ at 0.04582 m/s. The physical implication is that at lower flow rates, although the field enhances mixing, the increased viscous interaction with the wall dominates, raising entropy. Additionally, higher nanoparticle concentrations increase viscosity and shear, leading to more entropy, while lower concentrations like 0.1 vol% yield relatively smaller values ($\sim 4.70 \times 10^{-9}$).

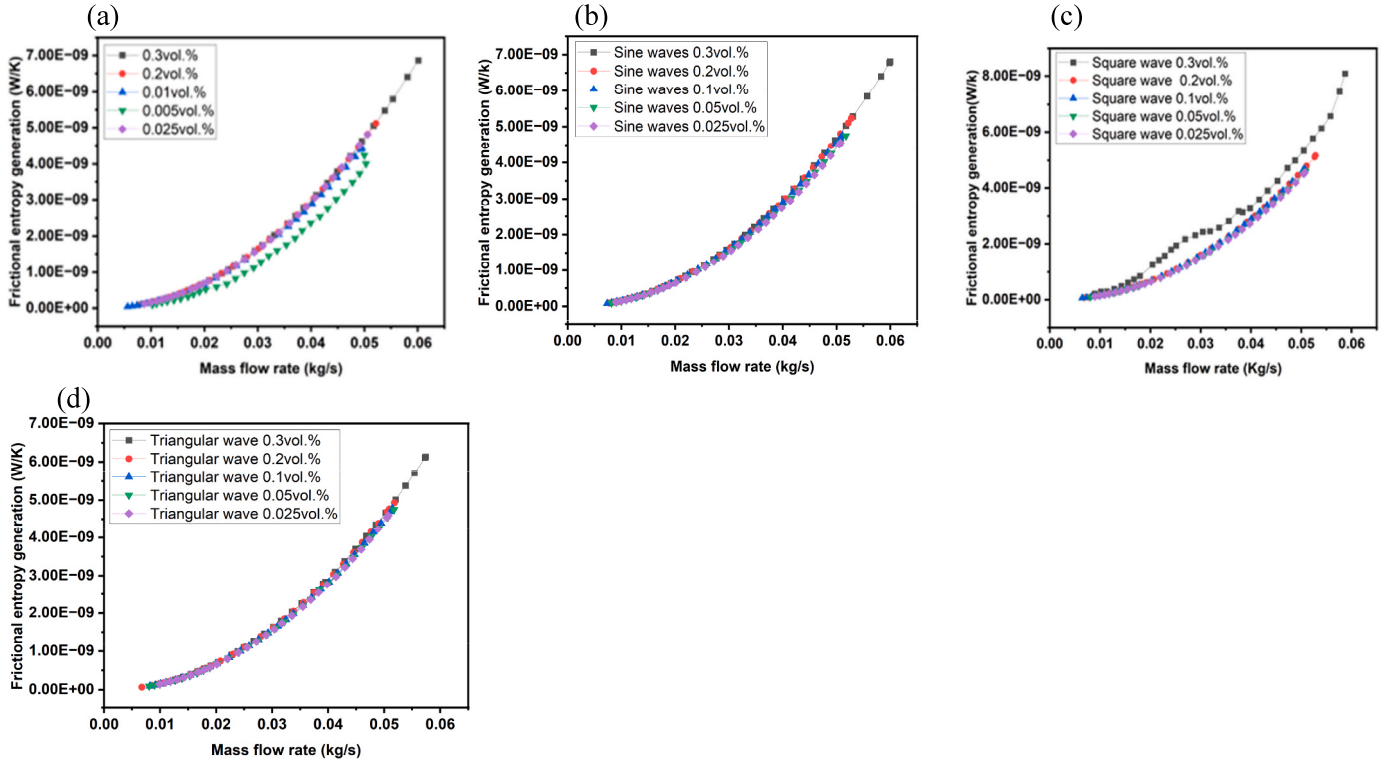


Fig. 16. a: Frictional entropy generation at various nanoparticle concentrations and flow rates (b) Frictional entropy generation under sine wave magnetic field (c) Frictional entropy generation under square wave magnetic field (d) Frictional entropy generation under triangular wave magnetic field.

Under a square wave magnetic field (Fig. 16c), the on/off nature of the waveform creates sharp transitions in the magnetic force, leading to more intense, instantaneous mixing and higher wall shear stresses. This results in substantially elevated entropy generation, especially at higher nanoparticle concentrations. For instance, at 0.3 vol% and 0.05872 m/s, entropy generation reaches $\sim 7.02 \times 10^{-6}$—several orders of magnitude higher than at lower concentrations (e.g., 0.2 vol% with $\sim 5.16 \times 10^{-9}$). This drastic rise in entropy illustrates how abrupt magnetic field transitions exacerbate energy losses due to turbulent flow interactions. However, as flow rates decrease, these disruptive effects diminish, resulting in lower entropy generation across concentrations this align with exiting study [69].

Triangular wave magnetic fields (Fig. 16d) produce a smoother oscillatory force, allowing more gradual and continuous modulation of the flow. As a result, the entropy generation decreases more predictably with flow rate reduction. For a 0.3 vol% nanofluid, entropy falls from $\sim 6.14 \times 10^{-9}$ at 0.05741 m/s to $\sim 1.30 \times 10^{-10}$ at 0.00909 m/s. The smoother waveform seems to reduce abrupt shear fluctuations, mitigating viscous losses while maintaining moderate enhancement in mixing. This trend holds for all concentrations, indicating that triangular waveforms strike a more favorable balance between enhanced heat transfer and reduced entropy generation.

Notably, higher nanoparticle concentrations consistently correlate with greater entropy values across all field types. This is due to the increased effective viscosity and enhanced momentum exchange in the fluid, which contribute to larger shear stress gradients and higher dissipation rates.

In practical terms, frictional entropy generation quantifies how much mechanical energy is being irreversibly lost as heat within the system due to internal fluid resistance. While waveform magnetic fields can improve heat transfer by promoting chaotic mixing and boundary layer disruption, they simultaneously elevate entropy generation due to intensified wall friction particularly at high nanoparticle concentrations and specific waveform types. Therefore, optimizing magnetic field configuration and nanoparticle loading is essential for designing energy-efficient nanofluid-based systems, ensuring that gains in convective performance do not come at an unsustainable thermodynamic cost.

4.8. Trade-off analysis between heat transfer and pressure drop using TEI

Fig. 17 illustrates the concentration thermal efficiency index (TEI) curve, developed to evaluate the trade-offs between heat transfer enhancement and pressure drop penalties at various nanoparticle concentrations in both the transition and turbulent flow regimes. The TEI functions as a comprehensive performance indicator, mathematically formulated to reflect the equilibrium between thermal improvement and hydrodynamic cost. From the curve, the highest TEI value of 1.8115 is observed at a concentration of 0.3 vol%, signifying the optimal point for thermal-hydraulic performance.

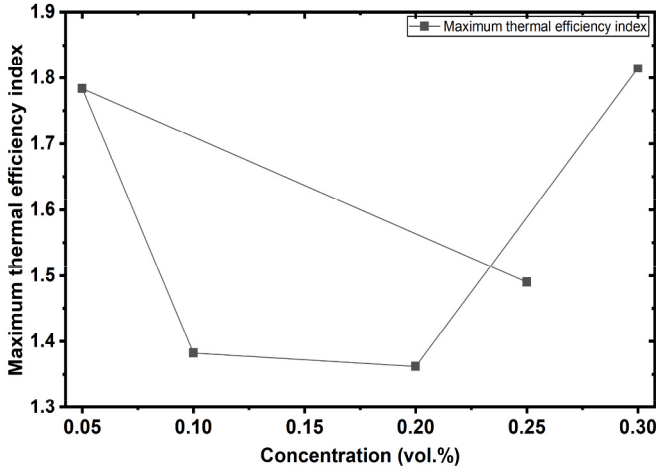


Fig. 17. Optimal concentration based on TEI

Physically, this denotes that at 0.3 vol%, the nanofluid delivers the most favorable balance between improved heat transfer and the associated increase in pumping power. At lower concentrations (e.g., 0.025–0.1 vol%), the enhancement in heat transfer is moderate but accompanied by minimal pressure drop, making them suitable for systems with limited pumping capacity. In contrast, while higher concentrations further improve thermal conductivity, the resulting viscosity increase leads to a disproportionately higher pressure drop, thereby diminishing overall system efficiency.

Thus, the TEI curve not only quantifies the trade-off mathematically but also identifies a practical operational sweet spot where the heat exchanger's effectiveness is maximized without incurring excessive energy consumption. These insights are particularly valuable for the optimal design and formulation of nanofluids in real-world applications such as compact heat exchangers, automotive cooling systems, and solar thermal collectors.

4.9. Comparison with heat transfer enhancement values from recent ternary or binary nanofluid studies

To contextualize the heat transfer performance observed in our study, Table 6 benchmarks key findings from recent experimental investigations involving ternary and binary hybrid nanofluids (THNFs). This comparison highlights the distinct advantage offered by magnetic waveform modulation in enhancing convective heat transfer.

The comparative data emphasize the novelty of your work: while previous studies such as Adun et al. and Mousavi et al. demonstrate static thermal or conductive property improvements, they do not explore dynamic flow modulation. Our experimental configuration, applying magnetic fields with tailored waveforms, not only achieves Nusselt number enhancements exceeding 39 % in the transition regime but also maintains a TEI above unity despite increased pressure drops indicating a favorable balance between enhanced heat transfer and pumping power penalty.

Moreover, the inclusion of MWCNTs furthers thermal conductivity and mixing efficiency, with entropic analysis affirming lower irreversibility under oscillatory magnetic forcing. Unlike the static or heat capacity–focused experiments in the reviewed literature, our work demonstrates practical heat exchanger relevance via controlled flow regime shifts and efficient energy transfer.

5. Conclusion and recommendation

This study experimentally demonstrates that the application of magnetic fields (MF) with varying waveform patterns significantly affects the thermal and flow behavior of Fe_3O_4-Al_2O_{33}–MWCNT ternary hybrid nanofluids (THNFs) in circular tubes, especially in the transition regime.

Key findings include.

- The use of THNFs without MF achieved a maximum Nusselt number enhancement of 29.49 % at 0.05 vol% in the transition regime. The optimal balance between heat transfer and pressure loss occurred at 0.3 vol%, where Nusselt number increased by 28.48 %, while maintaining a favorable pressure drop.
- Under magnetic modulation, square wave excitation delivered the highest convective heat transfer enhancement ranging from 26.68 % to 39.21 % in the transition regime and 7.89 %–18.42 % in turbulent flow. Sine and triangular waveforms followed closely with transition-regime enhancements of 26.11 %–35.5 % and 25.22 %–38.13 %, respectively.
- Despite increases in pressure drop (up to 2.5 × higher at 0.4 vol% compared to DIW), the Total Efficiency Index (TEI) remained >1

Table 6
Comparative experimental findings on binary and ternary hybrid nanofluids.

Study	Geometry & Conditions	Nanofluid Type	Key Outcomes	Insights Relative to Current Study
Adun et al. [33]	Static, 25–65 °C; volumetric fractions 0.5–1.25 %	$Fe_3O_4/Al_2O_3/ZnO/H_2O$ ternary hybrid	Specific heat capacity increase up to ~14.65 % at 25 °C and 1.25 vol %; stable dispersion confirmed	Complements our dynamic flow findings—heat capacity gains support potential for improved convective performance at low vol %
Mousavi et al. [68]	Static, 15–60 °C; 0.1–0.5 vol%	$CuO/MgO/TiO_2$ ternary hybrid nanofluid	Thermal conductivity and viscosity increased with concentration and temperature; optimal performance at CuO-rich mixture	Our Fe_3O_4/Al_2O_3/MWCNT shows significantly higher Nusselt improvements (up to ~39 %) under magnetic excitation, showcasing added benefit of MWCNTs
Muzaidi et al. [69]	Physical characterization	$CuO/SiO_2/TiO_2$ ternary hybrid	Volume fraction raised fluid density; XRD data confirmed hybrid formation	Reinforces structural robustness and stable hybrid formation seen in our fluid
Thanikodi et al. [70]	Evacuated tube solar collector; flow rates 1.5 & 3 L/min	Water-based tri-hybrid (MWCNT, Al_2O_3, MgO)	Thermal and exergy efficiency rose by ~19 % and ~32 % at higher flow rate, respectively	Echoes our flow-rate–dependent enhancements, now extended with magnetic waveform control
Sepehrnia et al. [71]	Hydraulic oil HLP 68, 0–1 vol%, 15–65 °C	Fe_3O_4/TiO_2/Graphene Oxide ternary hybrid	Viscosity increased by up to 1990 % at 15 °C; retained Newtonian behavior and exhibited high colloidal stability	While our viscosity increases are more moderate, the thermodynamic efficiency index (TEI >1) indicates effective heat transfer vs friction trade-off
Kanti et al. [72]	0.05–1 vol%, 30–60 °C	Graphene Oxide based binary & hybrid nanofluids	Thermal conductivity improved up to ~14.4 %; long-term stability; enhanced heat transfer above 45 °C	Our findings mirror these conductivity and stability benefits, while also leveraging waveform-driven mixing control
Fatih et al. [73]	Mixed convection; curved hot wall with impinging jets, rotating cylinder, MF (Ha = 0–20), inclination (0–90°), rotational speed (Ω = 0–2000), Richardson number (0.025–2.5)	Ternary nanofluid (not specified, assumed high-performance)	Higher Richardson number significantly reduced average Nusselt number, by up to 72 %. Cylinder rotation improved Nusselt number by 25.6 % over the stationary case. Flat wall with rotation gave 35 % better cooling than the curved wall. Magnetic field reduced cooling for both wall types. Increasing magnetic field inclination improved cooling by up to 29 %. Larger curvature aspect ratio lowered average Nusselt number by 39 %. Best and worst scenarios differed in performance by 143 %.	Highlights combined impact of jet dynamics, magnetic inclination, and wall curvature, offering insight into optimizing geometrical and MF parameters complementary to our waveform-based magnetic field modulation approach
Current Study	Circular tube flow with/without magnetic fields; 0.05–0.4 vol%; transition & turbulent regimes	Fe_3O_4/ Al_2O_3/MWCNT ternary hybrid nanofluid	- Nusselt number: +29.49 % (no MF, 0.05 vol %)- Square-wave MF boost: up to +39.21 % (transition); up to +18.42 % (turbulent)- TEI stays >1 despite pressure drop up to 2.5 × - Square wave triggers earlier turbulence onset- MWCNTs enhance mixing and conductivity (viscosity and friction factor rise by 16–25 % at ≥0.3 vol %)- Entropy generation and exergy destruction are reduced under waveform excitation	Establishes magnetic waveform modulation as a powerful method for enhancing convective heat transfer, with thermodynamic efficiency and controlled flow-regime transitions

across all test cases, indicating that heat transfer improvements outweigh frictional penalties.

- Square wave excitation caused the earliest transition to turbulence, marked by reduced critical Reynolds numbers. This is due to rapid and strong magnetic force gradients that enhance velocity fluctuations and disturb the thermal boundary layer more effectively than sine and triangular waveforms.
- The presence of MWCNTs enhances thermal conductivity and mixing, but at higher volume fractions (≥0.3 vol%), viscosity increases significantly, resulting in a 16 %–25 % increase in friction factor compared to DIW, particularly in the transition regime.
- Entropy generation analysis revealed that waveform-induced mixing reduces both viscous and thermal irreversibility. As such, energy loss per unit of thermal energy removed decreased, confirming lower exergy destruction under oscillatory MFs, particularly at lower flow rates.

These results confirm that the integration of THNFs with magnetic waveform excitation can effectively enhance convective heat transfer in a thermodynamically efficient manner. The findings provide a quantitative foundation for implementing such systems in compact, energy-sensitive heat exchangers.

6. Future perspective

To advance this work, the following future directions are recommended.

1 Synergistic Optimization of Magnetic Field and Nanoparticle Loading

Further studies should target the optimal combination of MF intensity, waveform type, and nanoparticle concentration to maximize thermal performance while minimizing pressure loss. Experimental and AI-based optimization algorithms should support parametric analysis.

2. Exploration of Alternative Base Fluids and Nanoparticles

Future work should investigate other working fluids such as liquid metals, ionic liquids, or base oils, combined with high-conductivity nanoparticles. The impact of MF on fluids with different magnetic susceptibilities or viscosities would broaden practical application scopes,

including nuclear, aerospace, and solar thermal systems.

3. Integration of Numerical Simulations with Experimental Data

Coupling high-fidelity CFD models with entropy generation and TEI calculations can enable better prediction and control of thermal-fluid behavior under dynamic magnetic environments, especially for large-scale or industrial systems.

4. Development of Smart Thermal Systems

Real-time modulation of MF waveform based on sensor feedback could lead to adaptive heat exchangers that self-optimize thermal efficiency in response to changing load conditions.

5. Integration of real-time flow visualization or PIV techniques for deeper insight into velocity field behavior.

6. Application of the magnetic waveform concept to other geometries (e.g., coils, rectangular ducts).

CRediT authorship contribution statement

Victor O. Adogbeji: Writing – original draft, Formal analysis, Data curation, Conceptualization. **Tartibu Lagouge:** Writing – review & editing, Validation, Supervision, Software, Funding acquisition. **Mohsen Sharifpur:** Writing – review & editing, Validation, Supervision, Resources, Project administration, Methodology, Funding acquisition. **Josua P. Meyer:** Writing – review & editing, Validation, Supervision, Project administration, Methodology.

Declaration of competing interest

The authors affirm that they do not have any known monetary interests or personal relationships that might be perceived as influencing the work presented in this paper.

Symbols and Terms

AL_2O_3	Aluminium oxide nanoparticles
Au	Gold nanoparticles
C_p	Specific heat transfer
Co_2O_3	Cobalt (III) oxide nanoparticles
Cu	Copper nanoparticles
CuO	Copper oxide nanoparticles
CHT	Convective heat transfer
CNTs	Carbon nanotubes
DC	Direct current
Di	Internal diameter of the tube
DIW	Deionized water
DW	Distilled water
EC	Electrical conductivity
EG	Ethylene glycol
Fe_2O_3	Iron (III) oxide nanoparticles
Fe_3O_4	Iron (IV) oxide nanoparticles
GA	Gum Arabic
GMO	Graphene magnetite oxide
I	Current (Ampere)
MF	Magnetic fields
MHNFs	Magnetic hybrid nanofluids
MNFs	Magnetic nanofluids
MNPs	Magnetic nanoparticles
MWCNT	Multiwalled carbon nanoparticle
OEF	Overall efficiency factors
SF	Sedimentation Factor
SiO_2	Silicon oxide nanoparticles
T	Tesla
TC	Thermal conductivity
TCE	Thermoelectrical conductivity
THNFs	Tri-hybrid nanofluids
Ha	Hartmann numbers
HNFs	Hybrid nanofluids
TEM	Transmission electron microscopy
Ti O_2	Titanium oxide nanoparticles
TEI	Total efficiency index
UV–Vis	Ultra Violet-Visible
V	Voltage
x/d	Axial distance

Subscripts

avg	Average
bf	base fluid

C_p	Specific heat capacity of particles (J/kg-K)
C_{pnf}	specific heat capacity of nanofluids (J/kg-K)
C_{pbf}	specific heat capacity of base fluids (J/kg-K)
C_{pnp}	specific heat capacity of nanoparticles (J/kg-K)
ρ_{nf}	Densities of the nanofluid (Kg /m^3)
ρ_{bf}	Density of base fluid (Kg /m^3)
$\varphi\rho_{np}$	Density of nanoparticles (Kg /m^3)
h_{avg}	Average heat transfer coefficient (W /m^2-K)
T_O	outlet °C
T_i	inlet °C
t_w	wall temperature °C
t_b	bulk temperature °C
n_f	nanofluid
n_p	nanoparticles

Dimensionless Numbers

Nu	Nusselt number
Re	Reynold number
Pr	Prandtl number

Greek symbols

φ	Mass ratio of nanofluids
Φ	Volume concentration (vol%)
μ	Viscosity (kg/m.s)
κ	Thermal conductivity (Wm/K-1)
σ	Electrical conductivity (mS/cm −1)
ρ	Density (Kg /m^3)
η	Thermal efficiency
$\dot{q}$	Heat flux, (W /m^2).

Data availability

Data is available upon request.

References

[1] V.O. Adogbeji, E.O. Atofarati, M. Sharifpur, J.P. Meyer, Magnetohydrodynamics of nanofluid internal forced convection: a review and outlook for practical applications, Results Phys. 68 (October 2024) (2025) 108082, https://doi.org/10.1016/j.rinp.2024.108082.

[2] S. Ahmad, H. Takana, K. Ali, Y. Akhtar, A.M. Hassan, A.E. Ragab, Role of localized magnetic field in vortex generation in tri-hybrid nanofluid flow: a numerical approach, Nanotechnol. Rev. 12 (1) (2023), https://doi.org/10.1515/ntrev-2022-0561.

[3] E.R. EL-Zahar, A.M. Rashad, W. Saad, L.F. Seddek, Magneto-hybrid nanofluids flow via mixed convection past a radiative circular cylinder, Sci. Rep. 10 (1) (2020) 1–13, https://doi.org/10.1038/s41598-020-66918-6.

[4] V.O. Adogbeji, M. Sharifpur, J.P. Meyer, International Journal of Thermal Sciences Experimental investigation of heat transfer , thermal efficiency , pressure drop , and flow characteristics of Fe 3 O 4 -MgO magnetic hybrid nanofluid in transitional flow regimes, Int. J. Therm. Sci. 209 (2025) 109515, https://doi.org/10.1016/j.ijthermalsci.2024.109515.

[5] J.P. Meyer, J.A. Olivier, Transitional flow inside enhanced tubes for fully developed and developing flow with different types of inlet disturbances: Part II-heat transfer, Int. J. Heat Mass Tran. 54 (7–8) (2011) 1598–1607, https://doi.org/10.1016/j.ijheatmasstransfer.2010.11.026.

[6] J.P. Meyer, S.M. Abolarin, Heat transfer and pressure drop in the transitional flow regime for a smooth circular tube with twisted tape inserts and a square-edged inlet, Int. J. Heat Mass Tran. 117 (2018) 11–29, https://doi.org/10.1016/j.ijheatmasstransfer.2017.09.103.

[7] B. Sun, Y. Guo, D. Yang, H. Li, The effect of constant magnetic field on convective heat transfer of Fe3O4/water magnetic nanofluid in horizontal circular tubes, Appl. Therm. Eng. 171 (May 2020), https://doi.org/10.1016/j.applthermaleng.2020.114920.

[8] M. Tekir, Experimental study on the thermal performance of hybrid nanofluid in a compact plate heat exchanger under the influence of a magnetic field, Case Stud. Therm. Eng. 69 (February) (2025) 106031, https://doi.org/10.1016/j.csite.2025.106031.

[9] F. Selimefendigil, H.F. Öztop, Coupled effects of corrugation and rotation on the phase transition and thermal process in a vented cavity under MHD convection, J. Energy Storage 77 (September 2023) (2024) 109925, https://doi.org/10.1016/j.est.2023.109925.

[10] F. Habiyaremye, M. Wainaina, The impact of the weak magnetic field on hydromagnetic nanofluid flow via divergent and convergent channels, Int. J. Fluid Mech. Therm. Sci. 10 (1) (2024) 15–24, https://doi.org/10.11648/j.ijfmts.20241001.12.

[11] A.S. Varkaneh, G.A.S. Nooshabadi, A.A.A. Arani, Flow field and heat transfer of ferromagnetic nanofluid in presence of magnetic field inside a corrugated tube, J. Therm. Eng. 9 (5) (2023) 1667–1686, https://doi.org/10.18186/THERMAL.1401685.

[12] M. Goharkhah, M. Ashjaee, M. Shahabadi, Experimental investigation on convective heat transfer and hydrodynamic characteristics of magnetite nanofluid under the influence of an alternating magnetic field, Int. J. Therm. Sci. 99 (Jan. 2016) 113–124, https://doi.org/10.1016/j.ijthermalsci.2015.08.008.

[13] M. Tekir, E. Taskesen, B. Aksu, E. Gedik, K. Arslan, Comparison of bi-directional multi-wave alternating magnetic field effect on ferromagnetic nanofluid flow in a circular pipe under laminar flow conditions, Appl. Therm. Eng. 179 (Oct) (2020), https://doi.org/10.1016/j.applthermaleng.2020.115624.

[14] D. Zheng, J. Yang, J. Wang, S. Kabelac, B. Sundén, Analyses of thermal performance and pressure drop in a plate heat exchanger filled with ferrofluids under a magnetic field, Fuel 293 (February) (2021) 1–9, https://doi.org/10.1016/j.fuel.2021.120432.

[15] S. Mei, C. Qi, T. Luo, X. Zhai, Y. Yan, Effects of magnetic field on thermo-hydraulic performance of Fe3O4-water nanofluids in a corrugated tube, Int. J. Heat Mass Tran. 128 (2019) 24–45, https://doi.org/10.1016/j.ijheatmasstransfer.2018.08.071.

[16] N. Hatami, A. Kazemnejad Banari, A. Malekzadeh, A.R. Pouranfard, The effect of magnetic field on nanofluids heat transfer through a uniformly heated horizontal tube, in: Physics Letters, Section A: General, Atomic and Solid State Physics, 381, Elsevier B.V, Feb. 05, 2017, pp. 510–515, https://doi.org/10.1016/j.physleta.2016.12.017, no. 5.

[17] J. Wang, G. Li, H. Zhu, J. Luo, B. Sundén, Experimental investigation on convective heat transfer of ferrofluids inside a pipe under various magnet orientations, Int. J. Heat Mass Tran. 132 (Apr. 2019) 407–419, https://doi.org/10.1016/j.ijheatmasstransfer.2018.12.023.

[18] D.Y. Aydın, E. Aydin, M. Gürü, The effects of particle mass fraction and static magnetic field on the thermal performance of NiFe2O4 nanofluid in a heat pipe, Int. J. Therm. Sci. 183 (March 2022) (2022) 107875, https://doi.org/10.1016/j.ijthermalsci.2022.107875.

[19] E. Taşkesen, M. Tekir, H.K. Pazarlıoğlu, M. Gurdal, E. Gedik, K. Arslan, The effect of MHD flow on hydrothermal characteristics of ferro-nano-fluid in circular pipe, Exp. Heat Transf. 36 (5) (2023) 617–631, https://doi.org/10.1080/08916152.2022.2065384.

[20] M. Amani, M. Ameri, A. Kasaeian, Investigating the convection heat transfer of Fe3O4 nanofluid in a porous metal foam tube under constant magnetic field, Exp.

Therm. Fluid Sci. 82 (Apr. 2017) 439–449, https://doi.org/10.1016/j.expthermflusci.2016.12.003.
[21] A. Lee, Y. Jeon, V. Chinnasamy, H. Cho, Investigation of forced convective heat transfer with magnetic field effect on water/ethylene glycol-cobalt zinc ferrite nanofluid, Int. Commun. Heat Mass Transf. 128 (October) (2021) 105647, https://doi.org/10.1016/j.icheatmasstransfer.2021.105647.
[22] M. Tekir, E. Taskesen, E. Gedik, K. Arslan, B. Aksu, Effect of constant magnetic field on Fe3O4-Cu/water hybrid nanofluid flow in a circular pipe, Heat Mass Transf. und Stoffuebertragung 58 (5) (May 2022) 707–717, https://doi.org/10.1007/s00231-021-03125-7.
[23] A. Shahsavar, M. Saghafian, M.R. Salimpour, M.B. Shafii, Experimental investigation on laminar forced convective heat transfer of ferrofluid loaded with carbon nanotubes under constant and alternating magnetic fields, Exp. Therm. Fluid Sci. 76 (Sep. 2016) 1–11, https://doi.org/10.1016/j.expthermflusci.2016.03.010.
[24] L. Shi, Y. Hu, Y. He, Magnetocontrollable convective heat transfer of nanofluid through a straight tube, Appl. Therm. Eng. 162 (Nov) (2019), https://doi.org/10.1016/j.applthermaleng.2019.114220.
[25] A. Javadpour, M. Najafi, K. Javaherdeh, Experimental investigation of forced convection heat transfer and friction factor of a non-Newtonian nanofluid flow through an annulus in the presence of magnetic field, J. Brazilian Soc. Mech. Sci. Eng. 40 (8) (Aug. 2018), https://doi.org/10.1007/s40430-018-1326-y.
[26] A. Javadpour, M. Najafi, K. Javaherdeh, Effect of magnetic field on forced convection heat transfer of a non-Newtonian nanofluid through an annulus: an experimental study, Heat Mass Transf. und Stoffuebertragung 54 (11) (Nov. 2018) 3307–3316, https://doi.org/10.1007/s00231-018-2361-z.
[27] J. Alsarraf, R. Rahmani, A. Shahsavar, M. Afrand, S. Wongwises, M.D. Tran, Effect of magnetic field on laminar forced convective heat transfer of MWCNT–Fe3O4/water hybrid nanofluid in a heated tube, J. Therm. Anal. Calorim. 137 (5) (Sep. 2019) 1809–1825, https://doi.org/10.1007/s10973-019-08078-y.
[28] E. Sadeghinezhad et al., "Experimental Study on Heat Transfer Augmentation of Graphene Based Ferrofluids in Presence of Magnetic Field", doi: 10.1016/j.applthermaleng.2016.11.199.
[29] M.S.Y. Ebaid, A.M. Ghrair, M. Al-busoul, Investigation of heat transfer enhancement using ferro-nanofluids (Fe3O4/water) in a heated pipe under the application of magnetic field, Adv. Mech. Eng. 14 (6) (Jun. 2022), https://doi.org/10.1177/16878132221102647.
[30] A.A. Karamallah, A. Habeeb Askar, L. Habeeb, The effect of magnetic field with nanofluid on heat transfer in a horizontal pipe investment cost analysis view project how to use engineering equation solver (EES): refrigeration and heat transfer applications view project the effect of magnetic field, Al-Khwarizmi Eng. J. 12 (3) (2016) 99–109.
[31] D. Guzei, A. Minakov, M. Pryazhnikov, and K. Meshkov, "Investigating the Forced Convection of Magnetic nanofluids.".
[32] X. Zhang, Y. Zhang, Experimental study on enhanced heat transfer and flow performance of magnetic nanofluids under alternating magnetic field, Int. J. Therm. Sci. 164 (January) (2021) 106897, https://doi.org/10.1016/j.ijthermalsci.2021.106897.
[33] H. Adun, D. Kavaz, I. Wole-Osho, M. Dagbasi, Synthesis of Fe3O4-Al2O3-ZnO/water ternary hybrid nanofluid: investigating the effects of temperature, volume concentration and mixture ratio on Specific heat capacity, and development of Hybrid machine learning for prediction, J. Energy Storage 41 (July) (2021) 102947, https://doi.org/10.1016/j.est.2021.102947.
[34] V.O. Adogbeji, E.O. Atofarati, K. Govinder, M. Sharifpur, J.P. Meyer, Tri-hybrid nanofluids for thermal applications : stability , magneto-hydrodynamics , and machine learning prediction, Multiscale Multidiscip. Model. Exp. Des. 123 (2025), https://doi.org/10.1007/s41939-025-00968-z.
[35] V.O. Adogbeji, M. Sharifpur, J.P. Meyer, V.O. Adogbeji, M. Sharifpur, J.P. Meyer, Experimental investigation into heat transfer and flow characteristics of magnetic hybrid nanofluid (Fe 3 O 4/TiO 2) in turbulent region, Appl. Therm. Eng. 258 (PA) (2025) 124630, https://doi.org/10.1016/j.applthermaleng.2024.124630. *Appl. Therm. Eng.*, vol. 258, no. PA, p. 124630, 2025.
[36] V.O. Adogbeji, E.O. Atofarati, M. Sharifpur, J.P. Meyer, Experimental investigation and machine learning modelling of the effects of hybridization mixing ratio, nanoparticle type, and temperature on the thermophysical properties of Fe_3O_4/TiO_2, Fe_3O_4/MgO, and Fe_3O_4/ZnO DI water hybrid ferrofluids, J. Therm. Anal. Calorim. (2025).
[37] J. Çengel, A. Yunus, Afshin Ghajar, Heat and Mass Transfer in SI Units: Fundamentals and Applications, sixth ed., MCGraw Hill, 2020.
[38] Z. Khedaer, D. Ahmed, S. Al-Jawad, Investigation of morphological, optical, and antibacterial properties of hybrid ZnO-MWCNT prepared by sol-gel, J. Appl. Sci. Nanotechnol. 1 (2) (2021) 66–77, https://doi.org/10.53293/jasn.2021.11634.
[39] S. Yick, et al., The effects of plasma treatment on bacterial biofilm formation on vertically-aligned carbon nanotube arrays, RSC Adv. 5 (7) (2015) 5142–5148, https://doi.org/10.1039/c4ra08187k.
[40] A. Zaman, T.U. Rashid, M.A. Khan, M.M. Rahman, Preparation and characterization of multiwall carbon nanotube (MWCNT) reinforced chitosan nanocomposites: effect of gamma radiation, BioNanoScience 5 (1) (2015) 31–38, https://doi.org/10.1007/s12668-014-0159-0.
[41] L. Zhuang, W. Zhang, Y. Zhao, H. Shen, H. Lin, J. Liang, Preparation and characterization of Fe3O4 particles with novel nanosheets morphology and magnetochromatic property by a modified solvothermal method, Sci. Rep. 5 (2015) 1–6, https://doi.org/10.1038/srep09320.
[42] A.A. Mohammed, Z.T. Khodair, A.A. Khadom, Preparation and investigation of the structural properties of α-Al2O3 nanoparticles using the sol-gel method, Chem. Data Collect. 29 (2020) 100531, https://doi.org/10.1016/j.cdc.2020.100531.
[43] A. Arifutzzaman, A.F. Ismail, I.I. Yaacob, M.Z. Alam, A.A. Khan, Stability investigation of water based exfoliated graphene nanofluids, in: IOP Conference Series: Materials Science and Engineering, Institute of Physics Publishing, Mar. 2019, https://doi.org/10.1088/1757-899X/488/1/012002.
[44] S.S. Jyothirmayee, P. Baskar, T. Theres, K. Sabareesh, S. Das, S. Ramaprabhu, Investigation of structural stability, dispersion, viscosity, and conductive heat transfer properties of functionalized carbon nanotube based nanofluids, J. Phys. Chem. C 115 (2011) 16737–16744, https://doi.org/10.1021/jp201672p.
[45] R.R. Sahoo, Experimental study on the viscosity of hybrid nanofluid and development of a new correlation, Heat Mass Transf. und Stoffuebertragung 56 (11) (2020) 3023–3033, https://doi.org/10.1007/s00231-020-02915-9.
[46] S. Chakraborty, I. Sarkar, A. Ashok, I. Sengupta, S.K. Pal, S. Chakraborty, Thermo-physical properties of Cu-Zn-Al LDH nanofluid and its application in spray cooling, Appl. Therm. Eng. 141 (May) (2018) 339–351, https://doi.org/10.1016/j.applthermaleng.2018.05.114.
[47] S. Chakraborty, I. Sarkar, A. Ashok, I. Sengupta, S.K. Pal, S. Chakraborty, Synthesis of Cu-Al LDH nanofluid and its application in spray cooling heat transfer of a hot steel plate, Powder Technol. 335 (2018) 285–300, https://doi.org/10.1016/j.powtec.2018.05.004.
[48] S. Chakraborty, P.K. Panigrahi, Stability of nanofluid: a review, in: Applied Thermal Engineering, 174, Elsevier Ltd, Jun. 25, 2020, https://doi.org/10.1016/j.applthermaleng.2020.115259.
[49] V.O. Adogbeji, M. Sharifpur, J.P. Meyer, Experimental investigation of heat transfer enhancement, thermal efficiency, and pressure drop in forced convection of magnetic hybrid nanofluid (Fe_3O_4/TiO_2) under varied magnetic field strengths and waveforms, Case Stud. Therm. Eng. 63 (October) (2024) 105313, https://doi.org/10.1016/j.csite.2024.105313.
[50] H. Topallar, B. Karadag, Mechanism of micelle formation in sodium dodecyl sulfate and cetyltrimethylammonium bromide, J. Surfactants Deterg. 1 (1) (1998) 49–51, https://doi.org/10.1007/s11743-998-0007-5.
[51] K.K. Sharker, M.N. Islam, S. Das, Counterion effect on krafft temperature and related properties of octadecyltrimethylammonium bromide, J. Surfactants Deterg. 20 (4) (2017) 923–932, https://doi.org/10.1007/s11743-017-1957-5.
[52] M. Momin, C.N. Nwaokocha, M. Sharifpur, G. Cheraghian, J.P. Meyer, M.A. El-Rahman, Investigation of thermal and electrical properties of ternary composite nanofluids using MgO, ZnO, and MWCNT nanoparticles, Results Phys. 70 (December 2024) (2025) 108139, https://doi.org/10.1016/j.rinp.2025.108139.
[53] V.O. Adogbeji, T. Lagouge, O. Al, Synergistic effects of spiral tape inserts and magnetic hybrid nanofluids on heat transfer and entropy generation in transition flow regime List of symbols, Multiscale Multidiscip. Model. Exp. Des. (2025), https://doi.org/10.1007/s41939-025-01012-w.
[54] M.T. Naik, L.S. Sundar, Heat transfer and friction factor with water/propylene glycol-based CuO nanofluid in circular tube with helical inserts under transition flow regime, Heat Transf. Eng. 35 (1) (Jan. 2014) 53–62, https://doi.org/10.1080/01457632.2013.810451.
[55] A.J. Ghajar, L.M. Tam, Heat transfer measurements and correlations in the transition region for a circular tube with three different inlet configurations, Exp. Therm. Fluid Sci. 8 (1) (1994) 79–90, https://doi.org/10.1016/0894-1777(94)90075-2.
[56] I.U. Ibrahim, M. Sharifpur, J.P. Meyer, S.M.S. Murshed, Experimental investigations of effects of nanoparticle size on force convective heat transfer characteristics of Al2O3 - MWCNT hybrid nanofluids in transitional flow regime, Int. J. Heat Mass Tran. 228 (June 2023) (2024) 125597, https://doi.org/10.1016/j.ijheatmasstransfer.2024.125597.
[57] G. Saha, M.C. Paul, Heat transfer and entropy generation of turbulent forced convection flow of nanofluids in a heated pipe, Int. Commun. Heat Mass Transf. 61 (2015) 26–36, https://doi.org/10.1016/j.icheatmasstransfer.2014.11.007.
[58] E.N. Sieder, G.E. Tate, Heat transfer and pressure drop of liquids in tubes, Ind. Eng. Chem. 28 (12) (1936) 1429–1435, https://doi.org/10.1021/ie50324a027.
[59] F.W. Dittus, L.M.K. Boelter, Heat transfer in automobile radiators of the tubular type, Int. Commun. Heat Mass Transf. 12 (1) (1985) 3–22, https://doi.org/10.1016/0735-1933(85)90003-X.
[60] V. Gnielinski, New equation for heat and mass transfer in turbulent and channel flow, Ind. Eng. Chem. Res. 16 (12) (1976) 359–368. https://cir.nii.ac.jp/crid/1571980075607043456.bib?lang=en.
[61] P.F. Dunn, Measurement and Data Analysis for Engineering and Science, second ed., Taylor and Francis/CRC Press, 2010, pp. 1–7, c 2010 ISBN : 9781439825686," no. August 2009.
[62] S. Osman, M. Sharifpur, J.P. Meyer, Experimental examination of transitional flow of dilute alumina - water nanofluid, in: International Heat Transfer Conference, Begell House Inc., 2018, pp. 3095–3102, https://doi.org/10.1615/ihtc16.cov.023235.
[63] J.P. Meyer, T.J. McKrell, K. Grote, The influence of multi-walled carbon nanotubes on single-phase heat transfer and pressure drop characteristics in the transitional flow regime of smooth tubes, Int. J. Heat Mass Tran. 58 (1–2) (2013) 597–609, https://doi.org/10.1016/j.ijheatmasstransfer.2012.11.074.
[64] M. Everts, J.P. Meyer, Heat transfer of developing and fully developed flow in smooth horizontal tubes in the transitional flow regime, Int. J. Heat Mass Tran. 117 (2018) 1331–1351, https://doi.org/10.1016/j.ijheatmasstransfer.2017.10.071.
[65] A.J. Ghajar, L.-M. Tam, Heat Transfer Measurements and Correlations in the Transition Region for a Circular Tube with Three Different Inlet Configurations, 1994.
[66] P.K. Kanti, V.V. Wanatasanappan, P. Sharma, N.M. Said, K.V. Sharma, Experimental and machine learning insights on heat transfer and friction factor analysis of novel hybrid nanofluids subjected to constant heat flux at various

mixture ratios, Int. J. Therm. Sci. 209 (August 2024) (2025) 109548, https://doi.org/10.1016/j.ijthermalsci.2024.109548.

[67] A.J. Chamkha, F. Selimefendigil, H.F. Oztop, MHD mixed convection and entropy generation in a lid-driven triangular cavity for various electrical conductivity models, Entropy 20 (12) (2018), https://doi.org/10.3390/e20120903.

[68] P.K. Kanti, et al., Thermal performance, entropy generation, and machine learning insights of Al_2O_3-TiO_2 hybrid nanofluids in turbulent flow, Sci. Rep. 15 (1) (2025) 1–20, https://doi.org/10.1038/s41598-025-93749-0.

[69] V.O. Adogbeji, K. Govinder, M. Sharifpur, J.P. Meyer, Experimental investigation of the effect of magnetic field placement on pressure drop , entropy generation , heat transfer , and thermal performance of Fe 3 O 4/TiO 2 magnetic nanofluids in turbulent flow, Powder Technol. 466 (July) (2025) 121504, https://doi.org/10.1016/j.powtec.2025.121504.

[70] S.M. Mousavi, F. Esmaeilzadeh, X.P. Wang, Effects of temperature and particles volume concentration on the thermophysical properties and the rheological behavior of CuO/MgO/TiO2 aqueous ternary hybrid nanofluid: experimental investigation, J. Therm. Anal. Calorim. 137 (3) (2019) 879–901, https://doi.org/10.1007/s10973-019-08006-0.

[71] N.A.S. Muzaidi, et al., Heat absorption properties of CuO/TiO2/SiO2 trihybrid nanofluids and its potential future direction towards solar thermal applications, Arab. J. Chem. 14 (4) (2021) 103059, https://doi.org/10.1016/j.arabjc.2021.103059.

[72] S. Thanikodi, J. Giri, R. Saravanan, S. Ahmad, A.O. Hourani, Case Studies in Thermal Engineering Thermal performance enhancement in evacuated tube solar collector with working fluid MWCNT/Al 2 O 3/MgO tri-hybrid nanofluid, Case Stud. Therm. Eng. 67 (September 2024) (2025) 105789, https://doi.org/10.1016/j.csite.2025.105789.

[73] M. Sepehrnia, A. Shahsavar, H. Maleki, A. Moradi, Experimental study on the dynamic viscosity of hydraulic oil HLP 68- Fe3O4-TiO2-GO ternary hybrid nanofluid and modeling utilizing machine learning technique, J. Taiwan Inst. Chem. Eng. 145 (Apr. 2023) 104841, https://doi.org/10.1016/J.JTICE.2023.104841.